Void Formation and Vacancy Injection in Silicon and Silicon Germanium

Void formation and vacancy injection in Silicon and Silicon Germanium

By

Han Z. Su, B.Eng.

A Thesis
Submitted to the School of Graduate Studies
in Partial Fulfillment of the Requirements
for the Degree of
Masters of Applied Science

McMaster University
Hamilton, Ontario, Canada

To my beloved Parents

MASTERS OF APPLIED SCIENCE (2006) McMASTER UNIVERSITY
(Electrical Engineering) Hamilton, Ontario, Canada

TITLE: Void formation and vacancy injection in Silicon and Silicon Germanium

AUTHOR: Han Z. Su, B.Eng. (McMaster University, Hamilton, Ontario, Canada)

SUPERVISOR: Dr. Y.M. Haddara and Dr. A.P. Knights

NUMBER OF PAGES: xv, 94

ABSTRACT

Substantial development of silicon-based technology is required to continue to improve product reliability and production yield of silicon-based IC devices. Defects play a key role in process technology and research is required into their properties and interactions with host and impurity atoms. Cavities formed by ion implantation of helium into a silicon substrate are known to be efficient gettering sites for mobile interstitials and metallic impurities. In addition, the existence of a buried void layer drastically reduces the unintentional parasitic transistor gain in power devices by introducing mid-gap energy levels in the substrate. Utilizing slow positron annihilation spectroscopy (PAS), void formation by implanted He^+ at a dose of $1\times10^{16}/cm^2$ and energy of 60 keV subsequently subjected to various annealing conditions, i.e. different temperatures, times, ramp rate and ambients, is reported. Quantitative measurement of cavity sizes shows that the annealing temperature largely influences helium out-diffusion from the implanted region. Consequently, different void evolution processes associated with specific annealing temperatures are found. Furthermore, larger voids are formed in oxygen ambient leading us to suggest that the supersaturation of interstitials enhances bubble migration and coalescence during the stage when a large fraction of He atoms remains in the cavities.

In recent years, SiGe pseudomorphic alloys have become attractive for heterostructure devices due to their higher mobility, lower noise and lower power consumption, as compared with traditional Si devices. More importantly, SiGe is highly compatible with Si processing technologies. With the continuous improvement of SiGe technology, it has been coupled with complementary metal oxide semiconductor (CMOS)

technology and has the potential to replace III-V compound semiconductor devices in the near future. However, many unknowns remain in this material system. The study of point defect injection during various thermal treatments is important in itself, and would also allow additional tools for the study of dopant diffusion in the material under different conditions. With preexistent voids in the buried substrate, we performed furnace wet oxidation on a $Si_{0.98}Ge_{0.08}$ sample at 900 °C for half an hour. A small shrinkage of the voids, as compared to complete annihilation in the case of inert annealing, signifies vacancy injection during the oxidation process. Possible defect generation mechanisms and difference in growth rate enhancement in dry and wet oxidation are discussed. Based on a literature review of Si and SiGe oxidation, we suggest that stress relaxation and the Si replacement mechanism are responsible for the catalytic effect of the oxide growth and the change of point defect generation.

ACKNOWLEDGEMENTS

First and foremost, I would like to express thanks and gratitude to my supervisors, Dr. Y. M. Haddara and Dr. A. P. Knights for their excellent supervision and instruction throughout the course of this work. Their kindness, encouragement, as well as invaluable advice provided the direction needed to make this work possible. I especially thank Dr. Haddara for his care, patience and support has made my experience at McMaster a pleasant one. I also express my sincerest gratefulness to Dr. Knights for his tutelage and expertise in positron annihilation that has made this research achievable.

I would also like to acknowledge Jim Garrett, Doris Stevanovic and Graham Pearson, without their help the experiments would have never been completed. Thanks also go to Karleen Dudeck for her time in preparing the TEM images.

Special thanks go to my colleagues, the past and present members of Dr. Yaser's research group, particularly, Ehab El-Badry, Mohamed Rabie, Ahmed Fakhr, Samer Rizk and Munir Eldesouki, for their help and support during the course of this work. My years at McMaster University shall remain the most enjoyable and memorable period. We have learned so much from each other.

Last but certainly not least, I am deeply grateful to my parents Ying Song Su and Gui Zhi Yang for their love and support. Words cannot express how proud I am to be their son. Thanks also go to my brother, my friend and my buddy Han Jin Su and his fiancée Jennifer Wai Chi Ip for their unwavering support. Additional thanks go to my cousin Min Yi Yang for her encouragement in all the times I needed.

TABLE OF CONTENTS

LIST OF FIGURES

LIST OF TABLES

LIST OF SYMBOLS AND ACRONYMS

γ	Photons annihilation ray
β^+	Positron
ψ	Positron penetration profile
α	Positron absorption coefficient for ^{22}Na
λ	Positron annihilation rate
Γ	Trapping coefficient of positron lifetime measurement
ρ	Mass density of substrate material
ν_e	Electron neutrino
Φ_I	Interstitial diffusivity correlation
ΦV	Vacancy diffusivity correlation
σ	Cavities standard deviation
$a_{Si_{1-x}Ge_x}$	SiGe lattice constant
A_0	Total area under the Doppler-Broadening Spectroscopy curve
A_S	Central area under the Doppler-Broadening Spectroscopy curve
A_W	Window area under the Doppler-Broadening Spectroscopy
ACAR	Angular correlation of annihilation radiation
ADC	Analogy-digital conversion
B	Parabolic rate constant
B/A	Linear rate constant
BiCMOS	Bipolar Complementary Metal Oxide Semiconductor
ΔC_I	Excess amount of interstitials
C	Speed of light
C_I^*	Interstitial equilibrium concentration
C_I	Interstitial concentration
Cl	Chlorine
C_O	Lattice concentration sites/cm^3
Co	Cobalt
CTR	Crystal truncation rod scattering
Cu	Copper
C_V^*	Vacancy equilibrium concentration
C_V	Vacancy concentration
Cz	Czochralski growth

d_m	Mean cavity diameter
d_I	Interstitial diffusivity
d_V	Vacancy diffusivity
D_o	Pre-exponential diffusion factory
D_S	Positron analysis sample density ($g.cm^{-3}$)
DOBS	Doppler-Broadening Spectroscopy
E	Positron analysis implantation energy
E_a	Diffusion activation energy
E_s	Positron energy window parameters for A_S
E_0	Positron annihilation energy 511 keV
E_1	Positron energy window parameters for A_W
E_2	Positron energy window parameters for A_W
$\overline{E}$	Mean positron source energy
FZ	Float-Zone growth
F	Fluorine
ΔG	Change of free energy
GaAs	Gallium Arsenide
GeO_2	Germanium dioxide
GRE	Growth rate enhancement
HBT	Heterojunction Bipolar Transistor
HCl	Hydrogen Chlorine
HD	High implanted dose
He	Helium
He_nV_m	Helium-vacancy complexes
H_I^f	Interstitial enthalpy formation energy
H_V^f	Vacancy enthalpy formation energy
I	Interstitial
IC	Integration Circuits
I_p	Positron intensities
InP	Indium Phosphide
k	Boltzmann's constant
k_p	Positron lifetime trapping rates
LD	Low implanted dose
LINAC	High-energy linear accelerator
LNT	Liquid nitrogen temperature

MBE	Molecular Beam Epitaxy
MD	Intermedium implanted dose
MOSFET	Metal Oxide Semiconductor Field Effect Transistor
MCA	Multi-channel analyzer
N_2	Nitrogen
Na	Sodium
Ne	Neon
NF_3	Nitrogen trifluoride
NH_3	Ammonia
O_2	Oxygen
OED	Oxidation enhanced diffusion
OR	Ostwald ripening
ORD	Oxidation retarded diffusion
OSF	Oxidation-induced stacking faults
PAS	Positron annihilation spectroscopy
PLS	Positron Lifetime Spectroscopy
ppm	Parts per million
Psec	Pico second
P_z	Momentum component of γ-ray propagation
q	Substrate average atomic number in positron analysis
Q_f	Fixed oxide charge density
Q_{it}	Interface trapped charge density
r	Radius of stacking fault
r_m	Cavity's mean radius
R_{gen}	Interstitial generation at the oxidizing interface
RT	Room temperature
RTA	Rapid thermal annealing
RTO	Rapid thermal oxidation
S_d	Entropy energy of a disorder system
S_V^f	Vacancy entropy formation energy
S_I^f	Interstitial entropy formation energy
SCCM	Standard cubic centimeters per minute
Si	Silicon
SiGe	Silicon Germanium
SiO_2	Silicon dioxide

SLM	Standard liters per minute
SRIM	Stopping and ranges of ions in matter
Δt	Positron lifetime
Δt_B	Defect free substrate positron lifetime
Δt_D	Defect related Positron lifetime
T	Absolute temperature
TCAD	Technology Computer Aided Design
TEM	Transmission Electron Microscope
T_i	Implantation temperature
ULSI	Ultra-Large Scale Integration
V	Vacancy
V_1	Single vacancies
V_2	Divacancies
V_c	Vacancy cluster concentration
VLSI	Very Large Scale Integration

Chapter 1

Introduction

1.1 Advantages of SiGe in semiconductor materials

The unique properties of semiconductor materials have made the wonder of our age. Through extensive studies in the past few decades mature semiconductor technologies have been established; especially the dominant silicon (Si) complementary metal oxide semiconductor (CMOS) process. Currently, millions of individual components can be integrated onto a single chip. In the last few years, CMOS scaling has reached a point where serious bottlenecks arise, and speed advantages may no longer be gained by merely shrinking the device. Innovative materials and new transistor structures are desirable in order to continue the historic progress of the electronic era, and the proposal of silicon germanium (SiGe) heterostructures is one of the best alternatives.

The silicon integration process has been the dominant technology in the semiconductor industry and is likely to remain in this leading position in the foreseeable future. Nonetheless, neither the first development of transistors by Bardeen, Brattain and Shockley of Bell Laboratories, nor the first invention of integrated circuits by Jack Kilby of Texas Instruments was using Si. In fact, both designs were fabricated with Ge. However, Ge was rapidly replaced by Si in the early 1960s due to the advantages of Si in the fabrication processes. The primary advantage of Si is that it is extremely abundant and easily purified. Secondly, the larger bandgap of Si (1.12 eV) results in smaller current leakages and allows Si devices to operate at higher temperatures than Ge (Eg =

0.66 eV) transistors. Thirdly, high quality Silicon dioxide (SiO_2) that is used in isolation, passivation or gate dielectric can be easily obtained by thermal growth of Si substrate, whereas a chemically stable Germanium dioxide (GeO_2) layer is difficult to form. It is found that GeO_2 formed by standard thermal oxidation is soluble in water, making it incompatible with IC fabrication steps [1]. As a result, Ge cannot compete with Si from the highly dense IC manufacturing standpoint.

Yet from a circuit designer's point of view, silicon is far from being an ideal semiconductor material. This is due to the low mobility, low saturation velocity and indirect bandgap of the substance. In contrast, many of the III-V compound semiconductors, such as GaAs and InP, that are composed of elements from group III and V in the periodic table do not suffer from these weaknesses. The high electron mobility of the III-V semiconductor results in the ability to achieve a high frequency response, a broad bandwidth and a large gain. This is ideal for analog circuits, especially in the area of radio frequency (RF) and microwave applications. In addition, the direct bandgap nature and the possibility of bandgap modification makes III-V alloys perfect systems for optical devices. However, accompanied with these benefits, III-V semiconductor devices suffer from mechanical fragility, higher defect density and poorer thermal conductivity compared with Si, and the lack of a robust thermally grown oxide. Combined, these defects drive up the cost of III-V fabrication technologies.

SiGe holds the promise of electrical properties similar to those of III-V semiconductors in a material that is compatible with conventional Si fabrication processes. Products using SiGe heterojunction bipolar transistors (HBTs) and SiGe in the source/drain regions of Si MOSFETs are already commercially available. The unique

properties of $Si_{1-x}Ge_x$ ($0 \leq x \leq 1$) have gained a lot of attention in recent years. A small lattice difference between the two elements, 4.2%, results in total miscibility in any alloy compositions (5.65Å and 5.43Å for Ge and Si respectively). The lattice constant in bulk $Si_{1-x}Ge_x$ varies according to the percentage of Ge and is mathematically predicted by Vegard's law [2]:

$$a_{Si_{1-x}Ge_x} = 0.5431 + 0.01992x + 0.0002733x^2 \text{ (nm)}. \quad (1.1)$$

If an epitaxial SiGe layer is grown on top of a Si substrate, also known as pseudomorphic growth, the thin film will be compressively strained; while if an epitaxial Si layer is grown on top of a relaxed SiGe substrate, a tensile strained Si layer will result. This is due to the continuity of the crystal structures of the two layers. A schematic diagram of the strains is shown in Figure 1.1. Nevertheless, the strained epitaxial layer is subjected to a stability criterion. In order to ensure the quality of the thin film during various fabrication processes, the alloy thickness can not exceed certain limits for a given Ge concentration. Figure 1.2 shows the stability curves of the critical thickness of SiGe versus Ge percentage. If the alloy thickness lies above the stability curve, the thin film is metastable and relaxations of the strained lattice will take place when the structure is exposed to temperatures above the growth temperature. In some cases, misfit dislocation might be formed.

The most important advantage of Si/SiGe heterostructures is that they allow both bandgap and strain engineering. The bandgap energy difference between Ge and Si is mainly due to the lattice difference between the two elements. By incorporating Ge into Si, a smaller bandgap than that of Si is obtained. It is known that the compressive strain within the alloy introduces additional bandgap shrinkage of approximately 75 meV for

each 10% Ge incorporated [3]. This band offset is primarily in the valence band. If a Si/SiGe/Si heterostructures is built as shown in Figure 1.3(a), a large band discontinuity on the valence band that confines holes is produced and a p-type quantum well is formed with a small quantum mechanical barrier to electrons in the conduction band. On the other hand, a tensile strained Si or $Si_{1-y}Ge_y$ layer must be deposited on a relaxed $Si_{1-x}Ge_x$ layer, where $x > y$, in order to have the electrons confined in the conduction band. This is illustrated in Figure 1.3 (b) as an n-type quantum well.

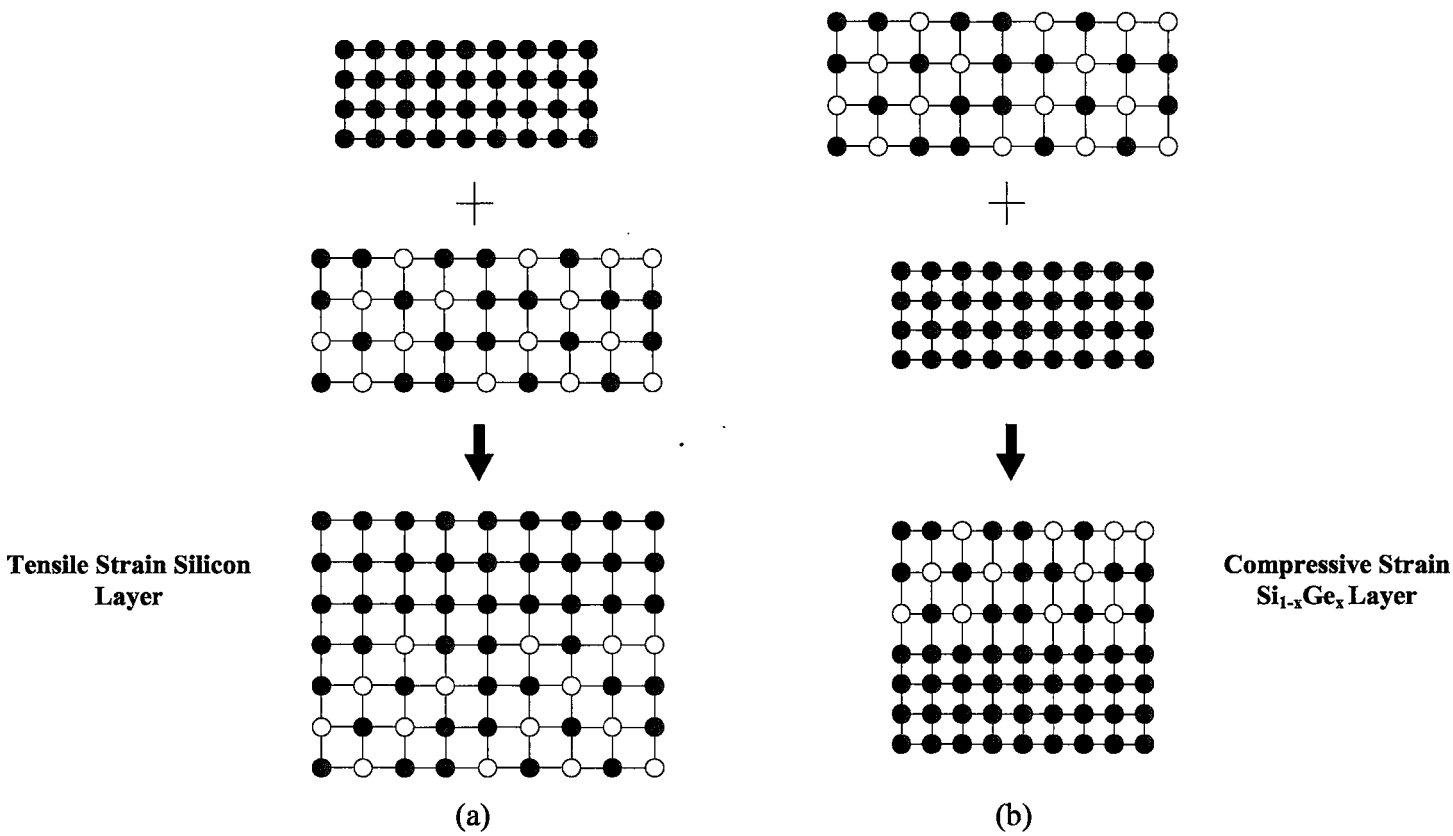

Figure 1.1. A schematic illustration tensile strained Si layer and compressive strained $Si_{1-x}Ge_x$ layer [1].

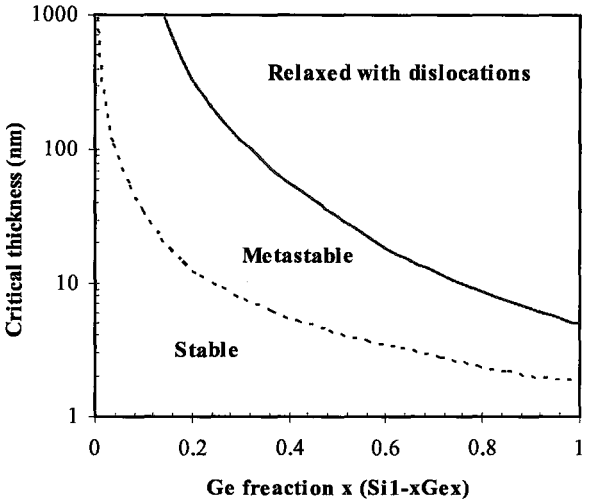

Figure 1.2. The Matthews and Blakesless pseudomorphic $Si_{1-x}Ge_x$ critical thickness vs. Ge content grown on bulk {100} silicon. A metastable curve for MBE growth also embedded [1].

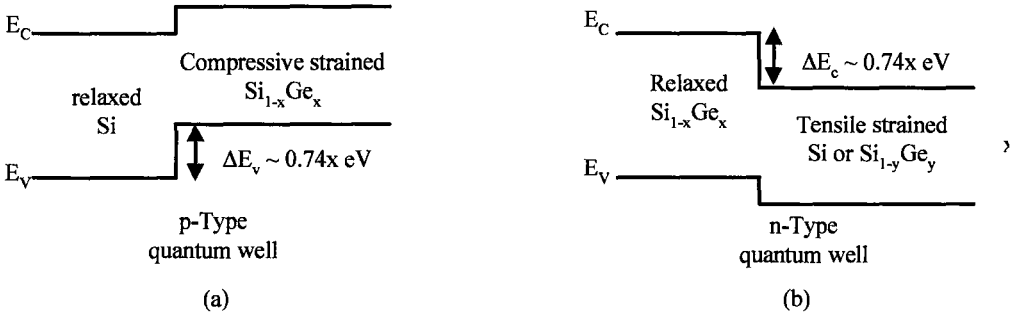

Figure 1.3. Band alignments and discontinuities of heterostructures (a) compressive strained $Si_{1-x}Ge_x$ forms a p-type quantum well for holes and (b) tensile strained Si or $Si_{1-y}Ge_y$ forms an n-type quantum well for electrons [1].

To date, SiGe HBT technology has proven to be a strong competitor with III-V HBT technology in the microelectronics market and the SiGe BiCMOS technology has been widely accepted in IC design. Strained SiGe in the source/drain region of MOSFETs has also moved into manufacture recently to reduce resistance and improve the drain induced barrier lowering (DIBL). Other application areas such as photo detectors, infrared detectors, optical modulators, optical routers, optical switching systems and Si/SiGe quantum cascade lasers have also been demonstrated to have the enormous potential to utilize SiGe technology [1].

This thesis focuses on issues related to the material properties of Si and SiGe as they relate to process technology. The focus is on point defects and their clusters since these play a key role in diffusion processes and device fabrication.

1.2 Motivation and Scope of the Study

This thesis focuses on two related phenomena, both of which are essential to studies of point defects, defect clusters, and defect-dopant interactions. The two phenomena are (1) void formation in silicon by helium implantation; and (2) point defect injection during oxidation of SiGe.

1.2.1 Void formation in silicon by helium implantation

Due to the dominant position of Si-based technologies, there continues to be much interest in understanding the physical phenomena involved in Si device fabrication, particularly those phenomena that affect yield and product reliability. It has been reported that due to its low solubility, ion implantion of He into silicon followed by high temperature annealing results in a layer of voids formed in the implanted region [4]. Recently, considerable attention has developed towards the applications of these nano-voids in silicon technology. For example, the interactions between voids and local defects or impurities in the substrate bulk have showed that voids are excellent sinks for mobile interstitials and are effective in gettering fast diffusing metals way from active device regions. From a process technology point of view, void formation is also important to understand as voids may be used to detect situations of point defect non-equilibrium, and

may therefore be used to probe phenomena related to defect-dopant interactions and dopant diffusion.

In spite of the great potentials of void applications in silicon technology, void formation under the effects of implant and annealing conditions are still not fully clear, particularly the voids evolution mechanism. Thus, further investigation on this topic is needed in order to have a better control of the technology. Moreover, voids were also utilized in our study of point defect injection during oxidation of SiGe. Therefore, understanding of void formation process would largely help us to interpret the results obtained by oxidation or inert anneal of SiGe.

1.2.2 Point defect generation under the effect of SiGe oxidation

Despite the great success of SiGe HBT and SiGe BiCMOS technologies in the semiconductor industry, there are still many unknowns in the SiGe fabrication process. Point defect injection during thermal oxidation of SiGe is certainly a key issue that needs to be clarified in this material system. It has been suggested that Si interstitial injection is suppressed and a vacancy flux into the substrate dominates in wet oxidation of SiGe alloys [5], but there are no direct experimental data supporting this hypothesis. In addition, disagreement continues about the source of the hypothesized vacancy flux [6], [7]. LeGoues *et al.* [6] suggested vacancies must be generated from the oxidizing interface in order to explain the observation of voids near the SiGe/Si interface. While Kilpatrick *et al.* [7] agreed that a flux of vacancies must be accompanied with the upward diffusion of Si atoms, they argued the source of these vacancies should be attributed to the Ge-rich/SiGe surface. In addition, a recent publication has shown that interstitials are suppressed at the

oxidizing interface of SiGe dry oxidation [5]. However, clear demonstration and physical evidence of the change of point defect generation (from interstitials to vacancies) has not been reported. Quantitative determination of the defect injected would allow studies probing the effect of point defect injection on the diffusion of various dopants, and hence allow the identification of dopant diffusion mechanisms in SiGe. A clear determination of these mechanisms would be of great value in incorporating SiGe in TCAD models for process simulators so that these simulators may reliably be used in SiGe technology development.

We have designed an experiment that employs voids in SiGe to detect the injection of interstitials and vacancies from the surface. The results of this study will give us a clear picture of the mechanism(s) of thermal oxidation of SiGe and enable us to accurately predict the phenomena that are associated with point defects. Cz SiGe with Ge content of 8% was used in the experiment. Vacancies were created by ion implantation of helium. High temperature wet oxidation was performed in conventional furnace under atmosphere pressure. Positron Annihilation Spectroscopy (PAS) was used to measure the change of voids, before and after annealing, which indicates the corresponding type of defect injected during annealing.

1.3 Thesis organization

This work is divided into seven chapters. This chapter serves as an introduction. The basic theory of intrinsic defects formation under equilibrium condition is given in chapter 2. The upward diffusion of Si atoms through the Ge-rich layer to the oxidizing

interface make it necessary to clarify the self-diffusion mechanisms of Si and SiGe. This is also included in chapter 2.

Chapter 3 discusses the kinetics of SiGe oxidation and presents a detailed investigation of the various factors that may affect point defect generation during Si oxidation. This is followed by a detailed investigation of void formation in Si substrate under ion implantation of Helium in chapter 4.

Experimental details such as sample preparation, oxidation/annealing conditions and sample analysis technique are fully described in chapter 5. Interpretations of the experimental results in chapter 6 are based on the theories given in chapter 3 and 4. We conclude in Chapter 7 with a summary of our contributions and a brief discussion of possible future research directions.

Chapter 2

Point Defects and Self-diffusion in Si and SiGe

2.1 Introduction

The influence of point defects in Silicon based devices has been extensively studied in the past few decades [11]. Due to the continuous shrinkage of IC devices and the critical roles played by point defects in fabrication processes, a deeper level of understanding of point defects and their associated phenomena is needed. Dopant diffusion is mainly attributed to the point defect concentration within the crystal structure. The excess point defects often lead to enhanced or retarded dopants diffusion, which significantly alters the geometrical design of a device. All these may result in the degradation of the device performance. As a result, much interest has been directed at the study of point defects and their interaction with dopants in semiconductors.

2.2 Point Defects

In an ideal crystalline material, atoms are arranged in an infinitely repetitive three dimensional pattern. This ideal situation of infinitely perfect repetition does not occur in reality. Imperfections always exist and point defects are among these imperfections. Other defects commonly found in crystalline materials include linear defects (also known as interfacial defects), boundary defects (also known as area defects) and volume defects. To clarify the basic difference between point defects and the other defects, the latter (linear, boundary and volume defects) are thermodynamically reversible. This means that

when structures are annealed in adequate temperatures and times in an inert ambient, the crystalline structure can be restored. On the other hand, point defects are thermodynamically irreversible.

In general, semiconductor point defects can be classified into two main categories: impurity defects and intrinsic native point defects. The impurity dopant defects are elements other than the host atom that are added to the lattice either intentionally (dopants that enhance the electrical properties of the material) or unintentionally (contaminants). On the other hand, intrinsic native point defects naturally exist in the crystal structure under conditions of thermodynamic equilibrium. There are two types of intrinsic point defects: vacancy and self-interstitial. A vacancy is defined as an atom missing from its original site leaving an empty site behind. In contrast, if an extra atom resides in a non-lattice site, a self-interstitial defect forms. We shall simply denote vacancy as V and interstitial as I throughout this work.

2.3 Surface defects generation

From the thermodynamic perspective, V can be generated by removing an atom from the bulk of the substrate and attaching it to a kink at the surface. This requires energy to break the bonds in the bulk, move the atom to the surface and form new bonds with the surface kinks. The total energy of this process is called the formation energy of the vacancy (H_V^f) and it is pressure and temperature dependent. Similarly for the self-interstitial generation, an atom can be taken from a surface kink and placed into a non-lattice site of the substrate bulk. The interstitial formation energy is denoted as H_I^f. These

dual defect generation processes are known as the Schottky processes and they are assumed to be independent of each other. Hence, under equilibrium condition, the *I* concentration is not necessarily equal to the *V* concentration near the surface.

The change of free energy ΔG of a system can be described as:

$$\Delta G_x = n(H_x^f - TS_x^f) - TS_d, \tag{2.1}$$

where n is the number of defects of type X (X = *V* or *I*) in the system, and H_x^f and S_x^f are the enthalpy and entropy of formation for the defect (*V* or *I*). S_d is the disorder entropy. From the above equation, the total free energy change due to Schottky defects can be given by $\Delta G_V + \Delta G_I$ and under equilibrium conditions, defect (*I* & *V*) concentration can be expressed as:

$$C_V^* = C_O \exp\left[\frac{S_V^f}{k}\right] \exp\left[\frac{-H_V^f}{kT}\right], \tag{2.2}$$

and

$$C_I^* = C_O \exp\left[\frac{S_I^f}{k}\right] \exp\left[\frac{-H_I^f}{kT}\right], \tag{2.3}$$

where C_O is the number of lattice sites/cm^3.

2.4 Bulk defects generation

While the Schottky defect generation processes at the surface are assumed to be independent of each other, in bulk generation both *I* and *V* defects simultaneously form as an atom leaves its lattice site. Thus *I* and *V* concentrations must be the same wherever bulk generation dominates. Bulk generation is also known as the Frenkel process and the

mathematical expression for the defects concentration is illustrated in Eq. 2.4. Intuitively, the entropy of a system is the same for the Frenkel process and the Schottky process. However, using Schwarz's inequality, it can be shown that the entropy given in Eq. 2.2 and 2.3 is larger than that of Eq. 2.4.

$$C_V^* = C_I^* = C_O \exp\left[\frac{S_V^f + S_I^f}{2k}\right]\exp\left[-\frac{H_V^f + H_I^f}{2kT}\right], \qquad (2.4)$$

In another words, the surface Schottky process is more efficient in terms of free energy reduction. Furthermore, the different defect creation mechanisms result in different defect concentrations near the surface and in the bulk region. However, local dynamical equilibrium can always be achieved after a sufficiently long time and it can be described by the law of mass action $C_I C_V = C_I^* C_V^*$ [12].

2.5 Self-diffusion in Si

Under equilibrium conditions, point defects randomly move from high concentration to low concentration within the crystalline structure which gives rise to diffusion. One can treat self-diffusion as a special case of dopant diffusion that occurs without creating distortion or carrying extract charge in the lattice. Self-diffusion of Si has been extensively studied since the mid-1960s and there has been some controversy as to the type of defect that dominates the self-diffusion process.

It was first proposed by Seeger and Chik [13] that for temperatures above 900 °C, the self-diffusion mechanism in Si is governed by *I*; while below 900 °C, it is dominated by *V*. However, subsequent published data provided strong experimental evidence that both *I* and *V* are equally important in the diffusion process at temperature around 1000°C.

Two review papers by Fahey *et al.* [11] and Hu [14] point out that there is no clear definition of the type of defect that controls the Si self-diffusion mechanism, at least not in the temperature range around ~1000°C. However, they imply that at low temperatures vacancy is the dominant defect, while at high temperatures both *I* and *V* play an important role. The self-diffusion mechanism can be modeled by:

$$D_{self} = D_I + D_V = \Phi_I d_I \frac{C_I}{C_O} + \Phi_V d_V \frac{C_v}{C_O}, \tag{2.5}$$

where d_I and d_V are the diffusivities of *I* and *V* respectively. Φ_I and Φ_V are the correlation factors for the two defects.

The activation energy of Si self-diffusion varies from 3.9eV to 5.35eV in the temperature range of 700°C to 1385°C [11]. This large difference is a strong indication that a change over of diffusion mechanism occurs in going from low to high temperature, given that the diffusion energies for *V* and *I* in silicon are approximately equal to 4 and 5eV respectively [11], [14]. In addition, based on the observation of a non-Arrhenius break point, Fahey *et al.* [17] hypothesized that the transition of diffusion mechanism occurs at 1050°C. The experiment was performed using ^{71}Ge as a diffusion tracer due to its longer half life (11.2 days) as compared with ^{31}Si (2.6 hrs). This is possible since Ge and Si are both Group IV elements, and the size difference is relatively small. By extracting the diffusion profiles, Fahey *et al.* further suggested that at 1050°C, 60 to 70% of the self-diffusion mechanism is mediated by *V* and 30 to 40% is governed by *I*. However, the validity of using Ge as a tracer still needed to be verified.

^{30}Si and ^{29}Si were used as the isotope tracer profiles in a more recently study [15]. Non-equilibrium defect conditions were created through oxidation and nitridation in the temperature range between 1000 to 1100 °C. In addition, marker structures with layers

heavily doped with P and Sb were also used. By extrapolating the Si and the dopants diffusion profiles, Ural *et al.* [15] concluded that the self-diffusion mechanism is mediated approximately by one thirds of *V*, two thirds of *I*, and with the concerted exchange mechanism contributing less than 14%. In the following up study, Ural *et al.* [16] extended their investigation to a lower temperature (800°C), and as a result suggested that the *I* mediated fraction increases from 0.5 to 0.62 as the temperature increase from 800 to 1100 °C. They further deduced in this temperature range, the activation energies are 4.68 and 4.86 eV for *I* and *V* respectively. While the authors' interpretation of the data is arguable (particularly the suggestion of the concerted exchange mechanism), and while the results of Fahey [11] and Hu [14] continue to be more widely accepted, it is clear that the various studies converge on the fact that as temperature increases the *I* mediated fraction increases.

2.6 Self-diffusion in $Si_{1-x}Ge_x$

One of the advantages of SiGe is the total miscibility of Si and Ge in all alloy compositions, due to the small lattice difference between the two elements. To maintain the alloy composition and the lattice strain, the mechanism(s) that govern the self-diffusion process need to be well understood. Unlike silicon, SiGe self-diffusion has only been the subject of a limited number of publications [18]-[21]. The first investigation of Ge diffusion in polycrystalline SiGe was done by McVay *et al.*[18] in the temperature range of 900 to 1300 °C. The authors found that the activation energy drops rapidly as the Ge fraction is increased from 0 to 0.35, and then approaches a constant value of ~3 eV. This led McVay *et al.* to suggest that there is a changeover in the diffusion mechanism at Ge

percentage close 35%. In the Si-rich regime, the diffusion process is governed by both *I* and *V*, in a way similar to Si self-diffusion; whereas in the Ge-rich regime, *V* is the dominant defect.

Analogous diffusion profiles were also obtained in a recent investigation by ion implanted ^{71}Ge as a tracer in epitaxial SiGe alloys [19]. The annealing was done at temperatures between 894°C to 1263°C. Figure 2.1 shows the plots of activation energy, E_a, and pre-exponential factory, D_o, versus Ge fraction. By extrapolating from the diffusion data, Strohm *et al.* [19] found that a changeover point exists at Ge percentage close to 25%. This is lower than the value reported by McVay *et al.*, 35%. Furthermore, they recorded a higher activation energy at the break-point, (4.1 eV as compared to the 3.1 eV given by McVay *et al.*) and a continuous decrease in the activation energy as the Ge fraction increases after the break-point.

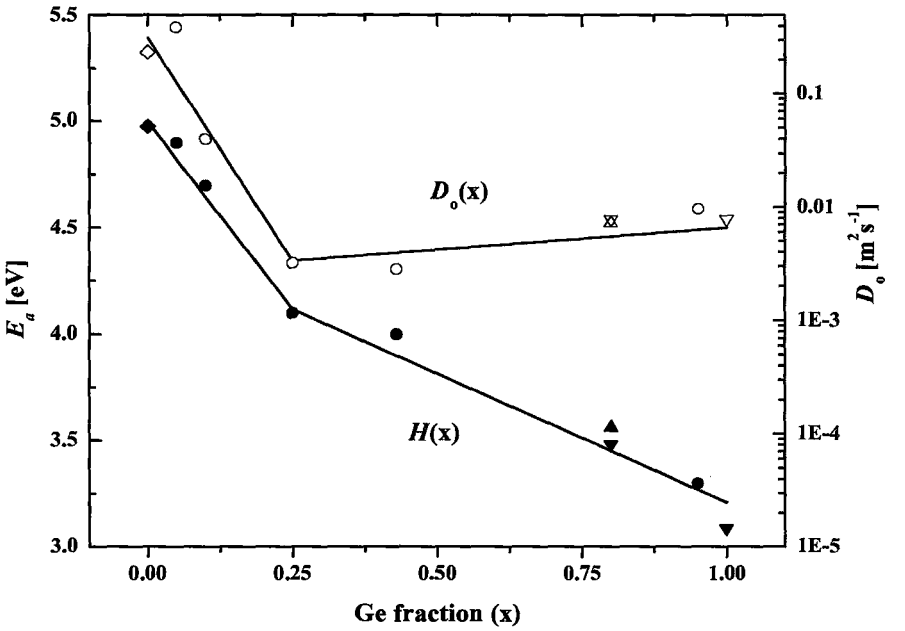

Figure 2.1 Activation Energy E_a and pre-exponential factors D_o for $Si_{1-x}Ge_x$ self-diffusion as functions of Ge content (filled and empty circles respectively). Diamonds: Ge in Si bulk; up-triangles: Si in $Si_{0.2}Ge_{0.8}$; down-triangles: Ge in $Si_{0.2}Ge_{0.8}$ and bulk Ge. [21]

Figure 2.1 also includes the diffusion data of Si and Ge diffused in $Si_{0.2}Ge_{0.8}$, in the temperature range of 860 to 950 °C [21]. The relatively low activation energy values led Laitinen *et al.* [21] to the conclusion that both elements are mediated by V in this high Ge fraction alloy. It can also be seen from the graph that the diffusivity of Ge is higher than Si in $Si_{0.2}Ge_{0.8}$. Laitinen *et al.* claimed that this is due to the different formation energies of V in the alloy. It was proposed that the formation energy of V varies linearly from 2 to 3 eV as a function of the number of Ge atoms on the nearest neighbor sites [22]. In other words, a higher number of Ge atoms in the vicinity site favors the formation of V defect. Therefore, it enhances the diffusion of Ge as compared to Si.

Recently, studies have shown that different strains in Si-rich alloy ($Si_{0.9}Ge_{0.1}$) significantly affect Ge diffusivity [20]. In the case of compressive strain, the diffusivity was reported to be enhanced (E_a = 4.33 eV); while for the substrate in tensile stain, the diffusivity found to be retarded (E_a = 4.90 eV). However, this was not seen on the Ge-rich end, indicating that the formation energy of V in Ge-rich alloy may not be affected by strain. A lower changeover point was also reported in the same study in relaxed SiGe alloy [20]. Zangenberg *et al.* suggested that vacancies start to take over the diffusion mechanism at Ge fraction as low as 20%. Furthermore, the self-diffusion profile was found to be close to Ge self-diffusion for Ge content large than 50%. Despite the inconsistencies on the changeover percentage and the diffusion activation energies amount different investigations, it is reasonable to conclude that the self-diffusivity of SiGe is a function of temperatures and alloy composition in which the V mediated fraction increases as the Ge percentage increases and the anneal temperature decreases.

Chapter 3

Literature Survey on Si and SiGe Oxidation

3.1 Introduction

Thermal oxidation of silicon is one of the most critical steps during any silicon microelectronic fabrication process due to the fact that silicon dioxide (SiO_2) is an excellent material for passivation, isolation, and gate dielectric. Although this topic has been extensively studied in the past few decades, the reaction at the atomic level near the interface is still under investigation. This is because of the difficulty in probing the interface and the short reaction time at the buried interface. It is well documented that the oxidation of silicon results in the injection of interstitials from the oxidizing interface [11], [14]. This influences dopant diffusion through several phenomena, including the formation of oxidation-induced stacking faults (OSF), oxidation-enhanced-diffusion (OED), or oxidation-retarded-diffusion (ORD). Therefore, it is very important to have a deep understanding of the point defects behavior under non-equilibrium conditions, in order to better control the fabrication process and minimize its negative impacts to the devices, both geometrically and electrically.

The injection of interstitials is mainly attributed to the stress relief and volume expansion of the newly formed oxide. The approximately 2.3 times volume increase of SiO_2 as compared to silicon is constrained by the silicon substrate in the lateral direction. This forces the newly formed oxide to expand only in the upward direction. However, as

the oxide thickness increases, the vertical expansion is also restricted by the covering oxide. The lateral stress thus created significantly influences the oxidation kinetics [23].

In the following sections of this chapter, the details of the defect generation mechanisms during thermal oxidation of silicon and their associated phenomena will be explored. The influences of different oxidation conditions are also examined. Finally, hypotheses regarding the effect of germanium on the oxidation of silicon germanium alloys will be summarized.

3.2 Thermal oxidation of Si

3.2.1 Stress accumulation at the oxidizing interface

Geometrically, the oxidation process proceeds layer by layer with oxygen atoms inserted into the bond-centered position of the Si atoms, forming Si-O-Si bonds. The lateral constraint and the vertical expansion restriction in the newly formed oxide result in considerable stress accumulation at the oxidizing interface

Since the late 1970's, there have been a number of important publications on the issue of stress induced during thermal oxidation [32]-[35]. This stress can be decomposed into two parts: mechanical stress and intrinsic stress. The mechanical stress can be understood as the difference between the linear thermal expansion coefficient of Si ($3.24 \times 10^{-6}/^{\circ}C$) and SiO_2 ($5 \times 10^{-7}/^{\circ}C$), while the intrinsic stress is the result of lattice mismatch between Si and SiO_2. It was observed by EerNisse [32] that during both dry and wet oxidation, at temperatures below 965 °C, silicon wafers tended to bend convex on the front surface as the oxide thickness increased. This led to the conclusion that as the

oxidation proceeds a large compressive stress accumulates in the oxide and a corresponding tensile stress accumulates in the silicon substrate. This bending was not observed for temperatures above 965 °C, indicating that for such high temperatures the stress is reduced or eliminated. In an earlier study EerNisse [36] had demonstrated that SiO_2 viscous flow occurs at temperatures as low as 960 °C. This viscous flow could account for the absence of interfacial stress at higher temperatures.

The finding of interfacial stress was further investigated by Charitat *et al.*[33] and Kobeda *et al.* [34], [35]. Both groups believed that the stress in the oxide was strongly related to the annealing temperature, time and ambient. By calculating the stress at room temperature, Kobeda *et al.* [35] found the intrinsic stress to exist at the interface even for temperatures above 1000 °C. Kobeda *et al* modeled the oxide viscous flow [36] and suggested that even at 1000 °C oxide viscous flow will require a finite time to effect stress relaxation at the interface. Kobeda *et al.* [35] predicted the stress relaxation time to be on the order of hundreds of seconds for temperatures close to 1000°C. This short relaxation time explains why oxide stress is not easily found at the oxidizing interface and in the bulk of the oxide layer after the oxidation process. Kobeda *et al.* [34] also discovered that the stress existing at the interface is substrate orientation dependent, following the order of {110} > {100} > {111}.

In the study of process parameters effect on stress, Hu [37] has demonstrated that a small amount of the hydroxyl content in the oxide layer can significantly decrease the stress and viscosity of oxide. This not only affects the oxidation rate but also influences the defect generation at the oxidizing interface. Incorporating fluorine or chlorine in the anneal ambient have similar effects on the oxidation rate and defect generation.

3.2.2 The effect of stress on oxidation rate

A number of investigations have suggested [39]~[43] that interfacial stress plays a significant role in the oxide growth rate. In a two-step oxidation study, Imai and Yamabe [40] found that subjecting a sample to a high temperature (1100 °C) inert anneal between two oxidation steps at low temperature (800 °C) yields a rate enhancement nearly four times during the second oxidation step. The rate of enhancement was explained by two factors: first, the intrinsic stress reduced from 1.4×10^9 dyne/cm^2 for the unannealed samples to 0.1×10^9 dyne/cm^2 for the annealed samples, and the stress state at the interface has a strong effect on the reaction kinetics. Second, the oxidant concentration in the oxide layer increased to over three times that of the unannealed samples. Similar conclusions were drawn in a recent publication by Gayathri and Banerjee [41].

3.2.3 Interstitial generation mechanics

The highly compressive stresses induced at the interface are due to the continuity of the crystalline structure and the large amount of free space required for SiO_2 volume expansion. The interface stress usually distorts the Si-O-Si bonding angles and causes the pseudo-crystalline structure to be unstable; hence, bonding reconstruction and injection of interstitials can easily take place. The energy advantage of Si emission, 2.4 eV, compared with the interstitial formation, 4.9 eV, clearly demonstrated this point [45].

It has been recognized by researchers that the injection of interstitials can relieve the interfacial stress by creating free volume. A group of scientists [29] in Japan utilized *ab initio* calculations to simulate the interface reaction at the atomic level and concluded that stress is the only reason causing the super-saturation of silicon self-interstitials in the

silicon bulk. They proposed that the compressive stress in the transition region from crystalline Si to amorphous SiO_2 is proportional to the number of O atoms inserted into the oxide network. Furthermore, by calculating the formation energy of Si emitted from the interface, it was shown that the emission not only releases the stress but also forms a more stable oxide structure as compared with the non-emitting model. Nevertheless, injection of interstitials from the interface can only supply a small amount of free volume and partially relax the accumulated stress; the larger portion is attributed to oxide viscous flow [45],[46]. It has been suggested that if self-interstitials were the only source for the stress relaxation, more than 30% [30] of the Si atoms must be ejected from the interface and the percentage increases to 55% for the case of free space formation [45]. These injection percentages would be inconsistent with the experimentally demonstrated fact that more than 99% of the Si is oxidized during the process.

3.2.4 The effect of viscosity and stress relaxation on point defect generation

In the Deal & Grove model [44], the oxide thickness can be accurately predicted by separating the oxidation into linear and parabolic regimes. However, the model is a macroscopic model that works well for thick oxides, and as such is not concerned with the atomistic mechanisms of the reaction.

Several workers have explored the atomistic mechanisms involved in Si oxidation and, particularly, phenomena involving point defects. Most authors (see, for example, Tan and Gösele [47] and Nicollian and Reisman [46],[48]) have proposed that viscous flow of the oxide formed is the rate-limiting step. Nicollian and Reisman distinguish between the reaction rate limited and diffusion limited cases, and their model successfully predicts

oxidation rate over a wide range of conditions. These studies maintain that the contribution of interstitials to the stress relaxation and free volume formation is minimal. A more recent oxidation model by Uematsu *et al.* [30] suggests that the oxidation rate is entirely dependent on the amount of self-interstitial injection into the oxide layer. They suggested that the rapid initial dry oxidation is because of the large amount of *I* injected into the oxide that can be easily oxidized there since there is less oxide viscous flow required for the free space formation. A break point of the *I* emission rate was found in Uematsu *et al.*'s model at temperatures close to 1000 °C for both dry and wet oxidation. This emission rate break point confirmed the viscoelastic properties of the oxide found by EerNisse *et al.* [36], which suggests that for temperatures above 960 °C interface stress significantly reduces and gives rise to a smaller flux of self-interstitials. Figure 3.1 shows the emission rate parameters used in the simulation of dry oxidation at different annealing temperatures.

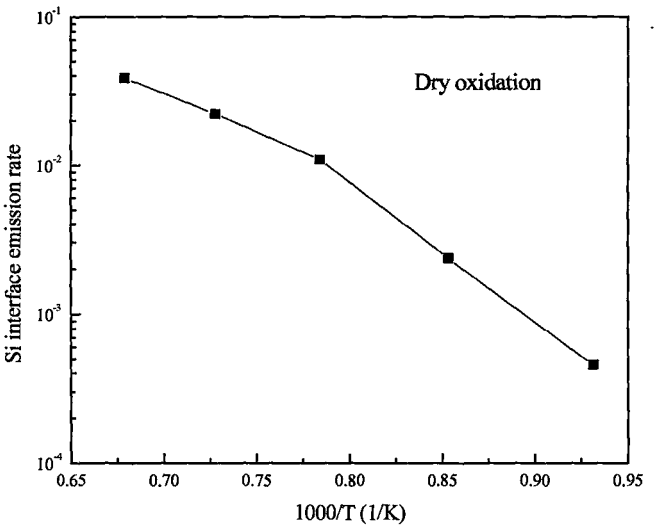

Figure 3.1. Modeling of Si self-emission rate vs. temperature during dry oxidation [30].

3.2.5 Point defect generation: the effect of fluorinated and chlorinated ambients

High quality oxides are desirable for VLSI circuit fabrication, especially for thin gate dielectrics. Such high quality oxides are usually produced in conventional tub furnaces at high temperatures using a dry oxidation ambient. In order to reduce the thermal budget while retaining the oxide quality, researchers have explored the addition of trace amounts of fluorine and/or chlorine compounds in the oxidation ambient. For example, it has been reported that fluorine in the range of parts per million incorporated into dry oxidation can significantly improve the dielectric strength and simultaneously enhance the oxidation rate. From the point of view of this thesis, the most relevant effect of chlorination and fluorination is the effect that these species have on point defect generation during oxidation. The results that we summarize here further strengthen our understanding that the stress state of the oxide layer is the primary factor controlling defect injection into the semiconductor substrate.

Fluorination (again in the range of ppm) has been found to result in a complete counter effect on dopant diffusion and the formation of stacking faults [50] - [53]. Rather than an injection of self-interstitials, it appears that a fluorinated dry oxidation injects vacancies into silicon. It also appears that the generation of vacancies is related both to the enhancement of the oxidation rate and the stress state of the oxide.

Kim *et al.* [51] suggest that the rate enhancement is caused by fluorine atoms reacting with the SiO_2 at the interface, which opens up the oxide structure by breaking Si-O-Si rings and randomly forms silicon monofluoride $Si(O^-)^3F$ or silicon difluorides $Si(O^-)^2F_2$. This causes the stress in the oxide layer and at the interface to relax significantly

therefore reducing the oxide viscous flow that is required for free space formation. Using pre-existing stacking-faults and a heavily doped marker structure, Kim *et al.* [50], [51], [53] observed defect emission from the interface change from interstitials to vacancies. They proposed that this change is primarily caused by the stress relaxation at the oxidizing interface. In addition, the OSF shrinkage activation energy during dry oxidation with incorporated fluorine is 1.7 eV, which is much less than in inert anneal, 4.8 eV [14], nitridation, 3.6 eV, and 3% HCl oxidation, 4.5 eV [53].

The higher bonding energy of Si-F, 5.8 eV, as compared to Si-O, 4.5 eV, results in the fluorine atoms being tightly bonded to the oxide network [52], so that a non-mobile and highly uniform concentration of fluorine profile was found throughout the oxide layer [51]. As the amount of NF_3 into the reaction increases, the optical index of refraction of the oxide layer was observed to decrease from 1.46 to 1.451 [51], which further confirms the structure relaxation takes place in the oxide layer. Figure 3.2 shows how the interfacial oxide stress varies versus different NF_3 concentrations and oxidation temperatures. Also incorporated into the figure is the stress for wet oxidation at 800 °C.

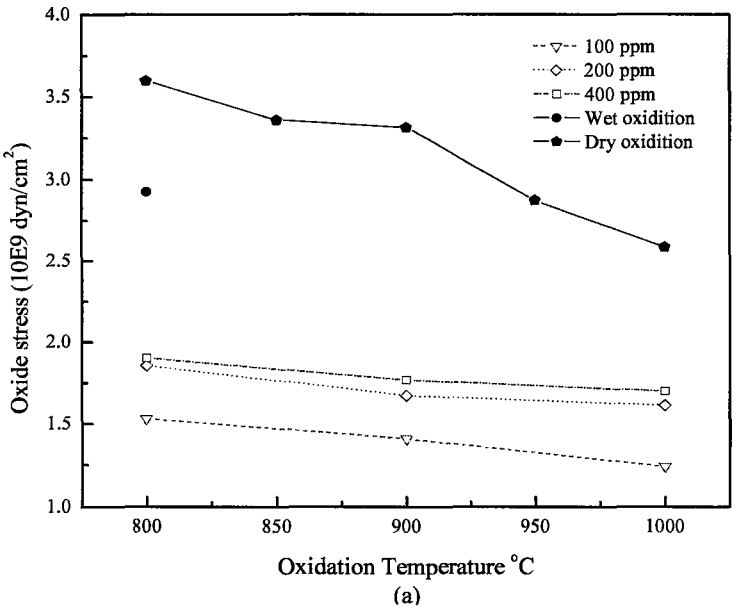

(a)

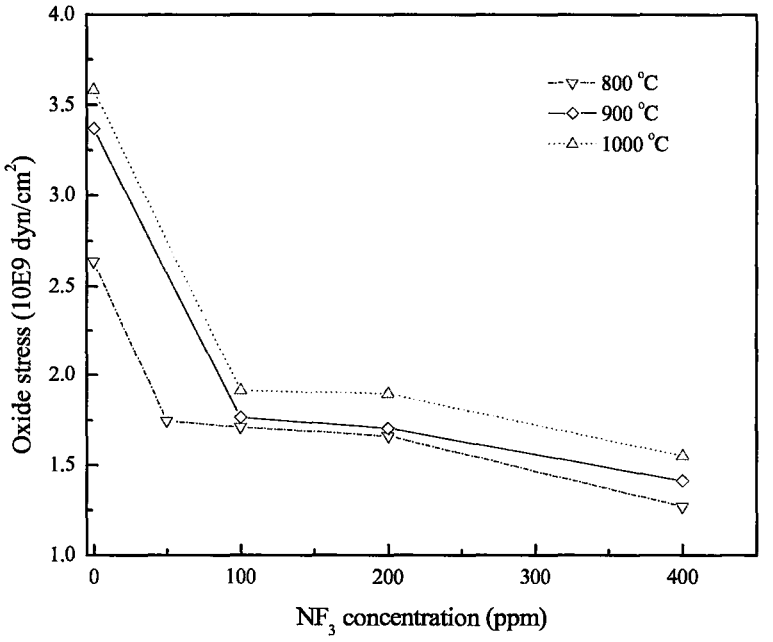

Figure 3.2. Relaxation of oxidizing interface stress by incorporation of NF_3 with substrate orientation {100} (a) stress vs. temperature, (b) stress vs. NF_3 concentration [38].

The incorporation of chlorine-containing species has similarly been shown to result in the suppression of Si interstitial injection, and thus lead to the retrogrowth of OSF [54]~[58]. The shrinkage rate of OSFs is directly proportional to the oxidation temperature and the fraction of the Cl-compound in the ambient. Above a certain temperature, complete annihilation of OSFs was found for a corresponding percentage of chlorine species in the mixed gases. As with the case of fluorination, there is an oxide growth rate enhancement (GRE) that accompanies the suppression of Si self-injection.

Vacancy supersaturation during the incorporation of chlorine species into dry oxidation is probably caused by the absorption of Si atoms at the oxidizing interface [55]. To explain the oxidation rate enhancement, it has been suggested that Cl-containing molecules diffuse through the oxide layer to react with Si atoms at the SiO_2/Si interface and form $SiCl_{2x}$. The $SiCl_{2x}$ molecules then diffuse back to the oxide layer and are

oxidized there because of the less stable Si-Cl bonds as compared with Si-O bonds. This hypothesis is supported by the observed pile-up of chlorine molecules in the oxide layer within 150 Å of the interface [54]. Additionally, in a recent *ab initio* study of the effect of H and Cl in dry oxidation, Uematsu *et al.* [58] proposed that the oxide viscous flow and the Si interstitial emission rate are significantly reduced (down to 75%) with the addition of 1% HCl. A further decrease of the self-emission rate was also noticed as the HCl volume percentage increases.

It should be pointed out here that if we accept this explanation of the effect of Cl it would indicate that both the stress reduction in the oxide and the injection of vacancies rather than interstitials are effects of the same cause (the absorption of silicon atoms via chemical reaction with chlorine) as opposed to the fluorination case where the injection of vacancies is a result of the stress reduction in the oxide layer. This indicates the different pathways by which changes in the oxidation kinetics can affect the injection of point defects.

3.2.6 The effect of surface recombination mechanisms on the quantity of excess interstitials

It has been shown that the growth rate of OSF is substrate orientation dependent which decreases following the order of {100}, {110} and {111} [14]. This decreasing pattern neither agrees with the oxidation growth rate order, nor the interface stress sequence. If the proposal that stress induces super-saturation of I is correct (section 3.2.1) or the oxidation rate dependence of the OSF growth is right (section 3.2.2), smallest OSF

size should be found in {100} orientation. In fact, the experimental data shows an opposite finding. This indicates that the OSF growth rate must involve other factors.

A kinetic model of interstitial injection during silicon oxidation was proposed by Hu [49] in the early 1970's. This was the first study relating both the phenomena of OED with OSF. Hu suggested that the injection rate is directly proportional to the oxidation rate. However, the super-saturation of interstitials at the oxidizing interface also causes surface re-growth and it is heavily dependent on the density of surface kinks of the substrate. The surface kinks density increases with the orientation orders of {100}, {110} and {111}, which is exactly the same trend as the OSF growth rate [49]. Moreover, stacking faults were observed in a {100} substrate during dry oxidation at 1200 °C, but none were found in the {10*l*} wafer. Hu [59] suggested that this was due to the extremely high density of surface kinks at the {10*l*} surface. It has been reported that small epitaxial regrowth Si islands formed by the ejected atoms were detected at the interface [61]. Hu [14] suggested that the kinks at the interface acted as recombination sites for interstitials, which significantly affect the growth of OSF and OED in the Si bulk. In addition, the surface states density of the oxide follows the same orientation order as the surface kinks density, increases with an increase in dangling bond density.

Hu suggested that the enormous amount of self-injection could yield simultaneous mono- and bi-molecular surface annihilation [62]. He divided the growth of OSF into three regimes: bimolecular annihilated, monatomic annihilated, and retrogrowth. Hu then proposed that the bimolecular mechanism dominates the surface re-construction process in the initial oxidation period. The large amount of interstitials injected from the interface increases the probability of two interstitial atoms neighboring each other, thus forming an

interstitial dimer. As the excess concentration of interstitials decreases with oxidation time, the probability of having two interstitial atoms bond together decreases. Hence, the bimolecular mechanism becomes negligibly small and the monatomic annihilation starts to take over. Figure 3.3 illustrates the three growth regimes of OSF.

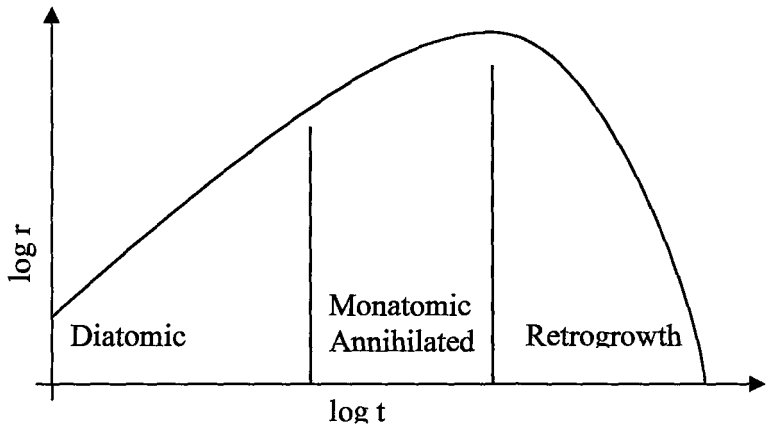

Figure 3.3. The three growth regimes of oxidation-induced stacking faults. [62]

In a recent investigation, Law *et al.* [63] adopted the idea of bimolecular re-growth in their study. The authors were able to explain the rapidly decaying length of OED over short lateral distances and the exponentially decaying length over long distances under various anneal temperatures. Compared with the single atom annihilation, it was found that bimolecular re-growth could be more effective in explaining the numerous inconsistencies between different experiments.

3.3 Thermal oxidation of $Si_{1-x}Ge_x$

The bandgap advantage and the compatibility with Si technology have increased interest in SiGe as a semiconductor material in recent years. In order to adopt this alloy material into highly integrated IC fabrication processes, a number of important studies on thermal oxidation of SiGe have been published throughout the last decade [5]-[8] ,[64]-[79]. It

has been reported that the presence of Ge at the oxidizing interface significantly alters the oxidation kinetics and perhaps the defect generation mechanism as well. In light of our foregoing review of Si oxidation and the associated defect injection phenomena it should be apparent that the way in which the presence of Ge modifies the oxidation kinetics can have a significant impact on defect generation both quantitatively and qualitatively. Much of the phenomena related to SiGe oxidation remain unclear. In this section we give a brief review of what is currently known with regards to SiGe oxidation kinetics. We then discuss possible defect generation mechanisms during SiGe oxidation. This will serve as adequate background to our own work on defect injection during SiGe oxidation, which we present in Chapter 6.

3.3.1 $Si_{1-x}Ge_x$ oxidation kinetics

The oxidation of $Si_{1-x}Ge_x$ is a considerably more complex process than that of pure Si. In wet oxidation, significant enhancement of the overall oxidation rate has been consistently observed. For dry oxidation, there is considerable debate about whether such an enhancement occurs at all, and if so whether it continues throughout the process or is limited to the initial rapid oxidation regime. Additionally, depending on the oxidation conditions the oxidation process may produce a pure SiO_2 or a mixed $(SiGe)O_2$. In the cases where a pure SiO_2 this may sometimes be accompanied by the formation of a Ge rich layer. There is as yet no consensus on a detailed physical explanation of all the relevant phenomena. Different authors have tried to explain some of the phenomena in terms of the weaker Si-Ge bond compared with the Si-Si bond, which would give rise to an increase in the number of Si^+ dangling bonds available for the formation of SiO_2 when

Ge is present; the larger atomic size of Ge, which would reduce the oxide/alloy interfacial stress; catalytic action by the Ge to provide a faster reaction path for the formation of SiO_2; or the upward diffusion of Si atoms, which would eliminate the possibility of Si self-injection (assuming such injection to be a rate limiting factor in Si oxidation).

Throughout the last decade, different kinetic models of $Si_{1-x}Ge_x$ oxidation have been proposed [7], [8], [65], [66]. By describing the oxide growth behaviors, authors attempted to accurately predict the Ge accumulation and the transition conditions from SiO_2 growth to mixed oxide formation. From the thermodynamic perspective, the free energies change in oxidation of silicon and germanium are $\Delta G_{Si} = -732$ and $\Delta G_{Ge} = -376$ kJ/mol O_2 respectively for the following reactions [65]:

$$Si + O_2 \rightarrow SiO_2, \tag{3.1}$$

$$Ge + O_2 \rightarrow GeO_2, \tag{3.2}$$

Both of the free energy values were obtained from the reaction at 1000 K. The large difference in the free energy of the reactions led Paine *et al.* [72] to suggest that only SiO_2 forms as long as there is an adequate amount of Si to participate in the reaction. They deduced that the critical mole fraction value should be around 3.22×10^{-19} (or 1.6×10^{4} atoms/cm^3), by which the alloy at the interface can be close to pure Ge. A similar suggestion was made by Frey *et al.* [67]. Instead of predicting the critical amount of Si atoms, Frey *et al.* formulated expressions to calculate the quantity of Ge accumulating at the interface, which triggers the incorporation of Ge into the oxide. The expressions were derived based on the difference between Si atoms consumed at the oxidizing interface and the Si flux diffusing through the Ge-rich layer. However, the outcome prediction of the transition oxide thickness did not perfectly match with experimental data. This is due

to a number of deficiencies in the model, such as neglecting the oxidant flux and the effect of Ge accumulation on the diffusivity of Si.

A more rigorous kinetic model was developed by Kilpatrick *et al.*[7]. The oxide transition formation is based on the competition of the oxidant flux diffusing through the oxide and the Si flux supplied from the substrate bulk. The deficiencies in Frey *et al.*'s model mentioned above were taken into account in Kilpatrick's work. They suggested that increases in the oxidation temperature and lower Ge content enhance the Si flux, which results in more favorable SiO_2 formation, while increase in the oxidant partial pressure and annealing the samples in a fast oxidation condition (wet ambient) causes the increase of oxidant flux, rendering a mixed oxide formation more probable.

The idea of a critical Si concentration present at the oxidizing interface to determine the mixed oxide formation (presented by Paine *et al.* [72]) is criticized by Hellberg *et al.*[65] [66]. They argued that this extremely low atomic concentration value cannot explain the experimental observation of the rapid formation of mixed oxides for Ge content larger than or equal to 50%. It also fails to explain the significant GRE of SiO_2 for Ge percentages less than 50%. Hellberg *et al.* suggested that silicon and germanium should simultaneously react with the oxidant to form SiO_2 and GeO_2 once the alloy is exposed to O_2 or H_2O. They claimed that the initial mixed oxide formation should occur for all alloy compositions. However, the thermal instability of GeO_2 as compared to SiO_2 gives rise to an almost immediate replacement reaction for annealing temperatures higher than 800 °C. It has also been demonstrated that the reduction of GeO_2 by Si takes place at temperatures as low as 200 °C [65] [reference therein]. The replacement mechanism is given by:

$$Si + GeO_2 \rightarrow SiO_2 + Ge, \quad (3.3)$$

The associated free energy change with the replacement reaction is $\Delta G_{Re} = -376$ kJ/mol O_2. Hellberg *et al.* argued that the instantaneous replacement mechanism following the simultaneous oxidation of Si and Ge should be primarily responsible for the large oxide GRE in wet oxidation. As for dry oxidation, the authors assumed that the incorporation of Ge into the reaction is negligible. Therefore, the replacement reaction is also insignificant which results in almost no growth rate enhancement. Hellberg *et al.* further suggested that the determination of the mixed oxide formation is dependent on several parameters: first, the amount of oxidant fluxes diffusing through the oxide layer. Second, the simultaneous formations of GeO_2 and SiO_2 at the oxidizing interface. Third, the opposite diffusion fluxes of Si and Ge in the alloy and in the Ge rich layer; and last, the replacement reaction of GeO_2 by Si.

A complete SiGe oxidation kinetic model was published recently [8]. By combining the idea of an oxidant flux competing with Si flux in Kilpatrick *et al.*'s work and the proposal of a replacement reaction in Hellberg *et al.*'s model, Rabie *et al.* [8] successfully described the SiGe oxidation behavior. The model accurately predicts the oxidation growth rate, the Ge pile-up and the mixed oxide transition conditions. Nonetheless, it is important to emphasize a key difference between the work of Hellberg *et al.* and Rabie *et al.*. While Hellberg *et al.* suggested that the replacement reaction occurs instantaneously, Rabie *et al.* argued that the reaction should occur at a finite rate. A thin GeO_2 layer found at the oxide surface for the $Si_{1-x}Ge_x$ ($x \leq 0.5$) samples oxidized at high temperatures ($\geq 1000^{\circ}C$) is a strong proof of this [68]-[70].

Until recently, the GRE was thought to be absent in the dry oxidation of $Si_{1-x}Ge_x$. In a high temperature (1000°C) rapid thermal dry oxidation study, a linear increase of the oxidation rate in the initial regime with an increase of the Ge content was observed by Terrasi *et al.* [68]. An enhancement factor of 2 was noticed for the Ge percentage at 30%. Based on the X-ray photoelectron spectroscopy and Rutherford backscattering spectrometry analysis, a small amount of GeO_2 was found in all alloy samples ($x \leq 0.3$). In addition, the quantity of Ge incorporated into the oxide is proportional to the initial SiGe composition, but with a reduction by a factor of 10. The formation of GeO_2 was also discovered in another investigation of rapid thermal dry oxidation [70]. However, the mixed oxide was only found to exist at the surface with a thickness equivalent to two mono-layers. Spadafora *et al.* [70] claimed that the surface GeO_2 formation resulted because of the relatively slow diffusion of Ge in the rapid thermal oxidation process as compared to standard furnace oxidation. This could be one of the explanations, but the phenomenon can also be interpreted as the reaction of Si with the instable GeO_2 is not instantaneous and that the fast oxidation front moves before the replacement mechanism.

The GRE in the thin oxide regime during the dry oxidation of $Si_{1-x}Ge_x$ is clearly illustrated in Figure 3.4. This proves that the Ge catalytic effect indeed exists in both of the dry and wet oxidation process, at least in the initial stage. To explain the GRE, Spadafora *et al.* [70] argued that the weaker Si-Ge bond might be one of the possibilities, but cannot be the complete solution of the phenomenon since the continuous accumulation of Ge does not further affect the growth. In fact, they have shown that a higher activation energy is required during SiGe oxidation as compared to Si. This indicates that the weaker Si-Ge bond is not an appropriate explanation of the GRE. In

addition, the irregular oxidation behavior shown in Figure 3.4 for the oxide thickness around 18 to 22 nm has led the authors to suggest that there must be a different oxidation kinetic in that regime which might be involved with a change in defect generation. We further explore this proposal below.

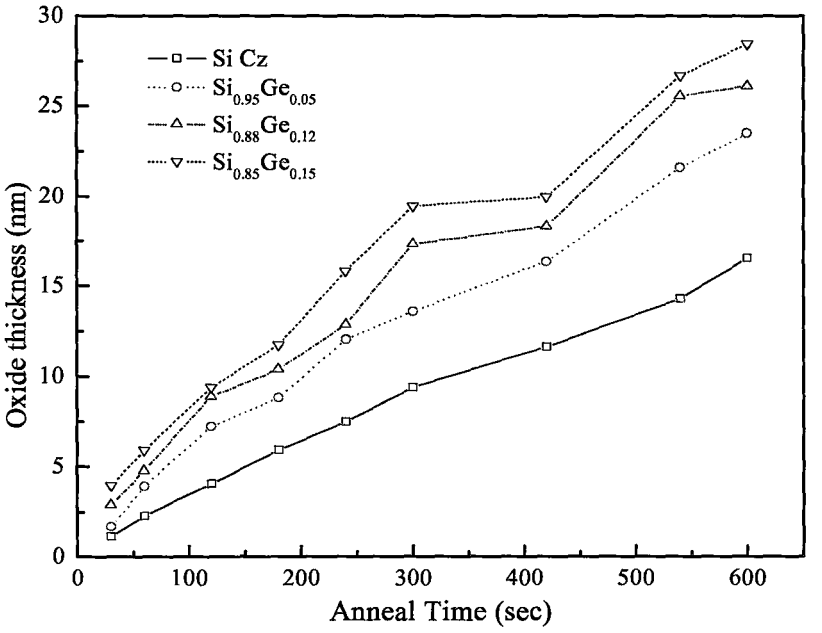

Figure 3.4. Oxide thickness vs. time during dry Rapid Thermal Oxidation (RTO) at 1000 °C [70].

3.3.2 Possible point defect injection during SiGe oxidation

It was suggested in an early study by LeGoues *et al.* [6] that the Ge catalytic effect is partially attributable to the suppression of Si interstitial injection. Due to the larger atomic size and the significant pile-up of Ge at the interface, the authors argued that point defect generation near the interface changes from the supersaturation of *I* known to occur during oxidation of pure Si to an excess of *V* in the oxidation of SiGe. They believed that the voids observed at the alloy/Si-substrate interface are due to the aggregation of injected *V*. The diffusion coefficients of Si and Ge are known to be higher in pure Ge

than in pure Si by several orders of magnitude. As Ge atoms pile-up at the interface, the self-diffusion of Si and Ge within the alloy changes rapidly, particularly in the enriched layer. This is because SiGe self-diffusion is a sensitive function of the local point defect density and the alloy composition (see section 2.6). LeGoues *et al.* suggested that the excess V assist the diffusion of Si atoms through the enriched layer to the SiO_2/SiGe interface to sustain the pure SiO_2 growth. In addition, they argued that the rate limiting term of wet Si oxidation is mainly the supersaturation of I, while for the case dry oxidation, other factor(s) (such as interface reaction) must responsible for the slow reaction. Hence, they concluded the generation of V in SiGe oxidation only affects the wet process.

The proposal of a change in the injected defect species in SiGe oxidation was also adopted by Kilpatrick *et al.* [7]. They reported that by incorporating 200 ppm of NF_3 into the dry oxidation ambient, GREs were observed in both of the Si and SiGe samples. The effect of fluorine addition in dry oxidation of Si was discussed in the previous section (3.2.5). The relatively larger increase of oxide growth in SiGe as compared to Si led Kilpatrick *et al.* to propose that there must be a parallel catalytic effect of F and Ge in the case of SiGe dry oxidation ($O_2 + NF_3$).

While they agreed that a vacancy supersaturation exists during SiGe oxidation, Kilpatrick *et al.* hypothesized that the source of vacancies is the Ge-rich/SiGe-alloy interface and not, as LeGoues *et al.* had suggested, the oxidizing interface. They pointed out that the small atomic volume increase from pure Si to mostly Ge is unlikely to cause total interfacial stress relief and V injection. Instead, the upward diffusion of Si atoms from the Ge-rich/SiGe interface most probably causes the supersaturation of V by leaving

empty sites behind. They suspected that the large amount of *I* emissions from the SiO_2/Ge-enriched interface still exists, but that only *I* defects are mostly Ge atoms. Since there is an absence of noticeable dislocation loops underneath the oxide, Kilpatrick *et al.* claimed that the injection of Ge atoms must undergo rapid recombination with the large *V* flux generated at the Ge-rich/SiGe interface. By adopting the interstitials enhanced diffusion model developed by Gösele and Tan [12], the authors further suggested that the Ge *I* fluxes are large enough to enhance Si diffusion through the enriched layer. To date, there is insufficient experimental and modeling work to resolve all these questions and the various hypotheses must be treated as tentative.

In Gösele and Tan's model, the *I* and *V* diffusion components in dopant diffusion [refer to equation (2.6) chapter 2] are key to determining the diffusion enhancement factor. If the interstitially-mediated component of the diffusion flux is small, then an extremely large excess of *I* is needed in order to have a small enhancement. The diffusion mechanism of Si in Ge-enriched alloys is largely attributed to *V* and the contribution percentage varies according to the alloy composition. Unfortunately, the precise fraction of *I* and *V* contributions to self-diffusion in SiGe have not been adequately investigated in the literature. Therefore, it is difficult to conclude whether the Ge *I* flux can result in a Si diffusion enhancement. Moreover, the observation of a perfectly epitaxial Ge enriched layer [6],[79] and the assumption of fast recombination of Ge *I* with the *V* fluxes from the Ge-rich/SiGe interface [7] indicates that the excess *I* would be limited, if any. In our opinion, the perfectly epitaxial Ge-enriched layer would contribute to the rapid surface annihilation of Ge atoms that are piled-up at the interface, similar to the surface annihilation of Si at the interface described in section 3.2.6.

A recent study has shown that a different defect injection mechanism may be involved following the formation of the Ge-enriched layer at the interface during dry oxidation of $Si_{1-x}Ge_x$ ($x \leq 0.15$) [79]. The thickness of the pseudomorphic SiGe layer was 11 nm. By extracting the diffusion profiles of two delta-shaped Boron doped spikes (about 100 and 300 nm below the surface), the supersaturation of I at the SiGe/Si interface was only found at the initial oxidation stage. It was found that the OED was completely suppressed after 20 minutes of annealing and the I concentration kept close to its equilibrium value even after the entire SiGe alloy had been consumed. The quantitative analysis of the I supersaturation rate is given in Figure 3.5. This finding of supersaturation of I at the initial oxidation regime agreed well with the investigation done by Spadafora *et al.* [70] in which small dislocations were observed at the SiGe/Si buffer interface after a short time rapid thermal anneal in dry O_2.

Regardless of the small atomic volume increase between Si and Ge, Napolitani *et al.* [79] suggested that the transient supersaturation of I in the initial oxidation regime is due to the process similarity between Si and SiGe. Comparing the plots in Figure 3.5, it is clearly shown that this short transient period is dependent on the Ge concentration. Based on the respective increase and decrease of I [79] [reference therein] and V [22] formation energies in Ge-rich alloys, Napolitani *et al.* hypothesized that either the excess I produced at the interface can not diffuse to the bulk region or are not produced at all after the Ge enriched layer is formed. Napolitani *et al.* claimed that the abnormal oxide growth behavior for the oxide thickness around 18 to 22 nm in Figure 3.4 is caused by the changes in point defect generation.

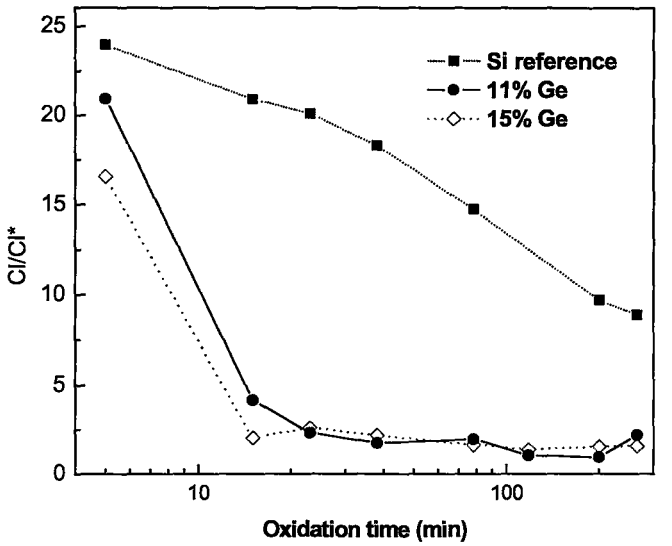

Figure 3.5. Interstitial supersaturation at the SiGe/Si interface vs. oxidation time at 815 °C for samples with an 11-nm SiGe cap layer at the surface. Pure Si reference sample also embedded in the graph [79].

In conclusion, extensive research on the oxidation of pure Si has demonstrated the intimate connection between the details of the oxidation reaction and the stress in the oxide layer on the one hand and point defect injection on the other hand. The oxidation of SiGe is a more complex process than the oxidation of pure Si. There is data to suggest that the presence of Ge affects both the stress in the oxide and the details of the chemical reactions at the interface. This leads us to expect that this would have a significant effect on point defect injection during SiGe oxidation. Some existing data suggest that there may be a change in the injected species. This in itself remains to be conclusively demonstrated. Additionally, if there is indeed vacancy injection during SiGe oxidation, the source of that injection flux is yet to be conclusively determined, and it remains to be understood whether any part of the structure would also contain a supersaturation of interstitials. In Chapter 6 we discuss our experimental contribution to addressing some of these questions.

Chapter 4

Void Formation in Silicon by Helium implantation

4.1 Introduction

The formation of gas bubbles in silicon after ion implantation of He is due to the very low solid solubility of the gas in the material, which is less than $1\times10^{16}/cm^3$. Depending on the implanted dose and energy, highly concentrated gas atoms within a damaged region could give rise to traps and act as nuclei for aggregation of small gas clusters in the as-implanted state. It has been demonstrated in perfect lattices that helium atoms tend to cluster together to reach a minimum energy configuration [9]. This suggests that the formation of small He clusters in the as-implanted state could start from agglomeration of interstitially trapped He atoms. Furthermore, the small clusters could interact with vacancies caused by the implantation and form small gas bubbles or He-vacancy (He_nV_m) complexes. However, depending on the He concentration and the subsequent annealing conditions, He clusters might also dissociate in the Si matrix. The release of He and the agglomeration of small bubbles occurs simultaneously as the annealing temperatures increase, often causing voids in the nanometer scale to appear after the process. Moreover, the inert property of the gas eliminates the possibility of chemical interaction with host atoms or other species in the substrate, which minimizes the potential to damage the designed structure on the substrate.

Recent studies have shown that voids are effective in the gettering of transition metals [10]. This is an important potential application in the development of new gettering

techniques in VLSI or ULSI technologies. In addition, the presence of voids in the buried layer introduces mid-gap energy levels in Si. It has been reported that two well defined tarp levels near the Si band gap (0.53 eV from the valence band for holes and 0.55 eV from the conduction band for electrons) have been detected [10]. This band gap modification abruptly decreases the unintentional parasitic transistor gain in ULSI design, by locally controlling the carrier lifetime. Other potential applications such as cavities in Si induce light emission or silicon-on-insulator structure produce by ion implantation of oxygen to form a buried oxide layer in the empty cavities region have also been reported [80], references therein.

In this work, our main interest in voids relates to their impact on point defect concentrations and hence diffusion and other process phenomena. This necessitates the development of detailed understanding of the nucleation and growth process of voids formation. In the following sections, the fundamental mechanisms of open volume defect (bubbles or cavities) and void formation on the atomic scale are explored. The correlation of void size with helium implanted and annealing conditions have been investigated in the literature. Throughout this dissertation we use "cavity" to refer to a bubble that contains helium, and "void" to refer to a bubble that does not contain any helium.

Void formation forms through the aggregation of He-V clusters followed by the outdiffusion of He. The next section discusses the formation and evolution of the He-V clusters. Section 4.3 discusses the outdiffusion of He and we conclude in Section 4.4 with a discussion of the effect of implant temperature.

4.2 He bubble formation and cluster evolution

Ion implantation commonly results in the formation of single vacancies (V_1) as vacancy-interstitial pairs result from the Frenkel reaction. In areas of high V_1 concentration, divacancies (V_2) or other larger open-volume defects appear as the clustering of V_1. In the as-implanted state, a certain amount of He is interstitially trapped in the damage region. To minimize the free energy of the system He atoms migrate to and fill the cavities. The passivation of divacancies or larger volume defects enhances the bubbles' stability and favors their evolution into more complex or larger clusters [10]. However, it is also known that the He atom is strongly repelled by V_1 due to the existence of negative electron repulsion [9]. Therefore, in the state where V_1 concentration is low, coarsening of large open-volume defects is reduced and V_1 can be easily annihilated with interstitial defects as the annealing temperatures increase. In addition, due to its high permeability in Si, He can easily escape from the substrate well below the Si melting temperature. It has been suggested that if small He bubbles are not formed in the as-implanted sample, no voids will be observed in the TEM images following a high temperature anneal [4]. Raineri *et al.* [4] suggested that the minimum concentration for void formation is 3.5 (±1) $\times 10^{20}$ cm^{-3}.

Void formation as functions of the implanted dose and the annealing temperature has been carefully investigated in the past decade [10]. Generally, the growth mechanisms can be classified into three different regimes according to the different implantation doses [83]: the low implanted dose regime ($<1\times10^{16}$ cm^{-2}), LD; the medium implanted dose regime ($\sim1\times10^{16}$ cm^{-2}), MD; and the high implanted dose regime ($>1\times10^{16}$ cm^{-2}), HD. Although implantation energies and temperatures also play important roles in void

evolution, they are relatively less significant when compared to the effect of the He implant dose.

In the LD regime, different layers can be found in the as-implanted sample according to their He-to-vacancy concentration ratio [81]. These include the surface layer with an abundance of V_I surrounded by a few He atoms; the intermedium layer with He_mV_n complexes resulting from the interaction between V_I and He; and the deepest implanted layer where the He-to-vacancy concentration ratio is very high due to the interstitial trapping of He atoms. Corni *et al.* [81] suggested that the strains measured by double crystal x-ray diffraction are most likely due to the existence of interstitially trapped He atoms. Indeed, as the annealing temperature increases the lattice strains disappear more rapidly. Raineri *et al.* [10] hypothesized that the extended depth of He atoms compared to the vacancy defects is attributed to the diffusion enhancement caused by the repulsive force between mono-vacancies and He atoms.

The recombination rate of the dilute and unstable V_I in the surface layer with the displaced Si atoms prevents the formation of large cavities in this region. In a slow positron annihilation spectroscopy study (implanted dose of 5×10^{15} cm^{-2}), Brusa *et al.* [82] reported that two thirds of the V_I were annihilated after a 150 °C anneal. However, at higher anneal temperatures He diffuses, resulting in a shift of the He profile from the deeper layer to the surface layer [81]. This allows both the mobile He atoms and V_I to affect the aggregation process, decreasing the clustering energy that is required for small bubble formation. Therefore, voids of the size of tetra-vacancies were detected by PAS [82]. However, these relatively small voids started to disappear at an anneal temperature of 700 °C and were totally annealed out at 900 °C [82]. In addition, interstitial clusters or

voids have not been reported in TEM measurements of LD samples before or after annealing.

For HD samples the He clustering efficiency increases with the increase of the implanted dose [10]. This combined with the larger damage resulting from the high dose implant result in the formation of dense small cavities with a mean diameter (d_m) up to 4 nm, which have been detected in as-implanted HD samples [83]. Post-annealing, a well-defined layer of voids in the damage region, with a $d_m \sim 8.5$ nm and a standard derivation (σ) of 4 nm, can be observed in TEM measurements [84].

The formation of interstitial defects (*I* defects), such as the {311} defects and the dislocation loops, in ion implanted Si has been extensively studied. The presence of extra impurity atoms in the lattice and the rapid annihilation of *V* at low temperatures (below 350 °C) result in supersaturation of *I* during the annealing process, which favors the formation of interstitial defects. However, the significant amount of *I* precipitation has not been observed in He-implanted samples in the HD regime ($>1\times10^{16}$ cm^{-2}). Roqueta *et al.* [85] hypothesized that the {311} defects detected in the first ten seconds of high temperature (800 °C) rapid thermal annealing (RTA) dissolve rapidly and recombine with small cavities within the first minute of annealing. Meanwhile, the coarsening of bubbles and the effusion of He occur simultaneously within the same characteristic time as the rapid dissolution of the *I* defects. Roqueta *et al.* further suggested the number of *I* defects that is required to reduce the size of a stable void is proportional to the square of the radius of the void (r^2). Thus, larger voids remain in the substrate even with the complete annihilation of *I* defects after a prolonged anneal.

Fukarek and Kaschny [80] have suggested that the over dense Si and small bubbles formation in the damage layer result in plastic flow deformation between implanted and non-implanted regions. In their study, a swelling step height of 3 nm was detected under atomic force microscopy (AFM) analysis for the as-implanted sample with a He implant dose of 5×10^{16} cm^{-2}. Subsequent to high temperature anneal, a step layer of 8 nm thick was measured [80]. In addition, the step height was found to increase linearly with the implanted dose [10].

While dissolution of interstitial clusters followed by the diffusion of interstitials to the surface and surface reconstruction may suffice to explain the step formation, Fukarek and Kaschny's interpretation is borne out by quantitative volume comparison indicating that there is a strong correlation between the amount of Si atoms in the step layer and the total voids generated in the buried layer after annealing [10]. It should be noted that such step layers have not been observed in LD and MD samples.

In the intermedium implanted dose regime, more complicated nucleation and structure evolution mechanisms are needed to describe the cavity growth phenomena. Clear visual evidence of small bubbles has not been observed in TEM images of as-implanted samples, but defects have been observed by TEM following high temperature treatment. A dilute system of planetary-like structures made up of a large central cavity surrounded by a number of small cavities is commonly seen in typical MD sample (1×10^{16} cm^{-2}) [83], [86], [87]. In addition, dislocation loops with strong strain field surrounding the planetary-like configuration have been reported both for rapid thermal and conventional furnace annealing [83], [86], [87]. This indicates that the cavity system is over-pressurized during thermal treatment. Fichtner *et al.* [83] proposed that the presence

of over-pressurized bubbles is most probably due to the very high He-to-vacancy ratio, implying that the limited amount of *V* cannot sustain the volume expansion requirement in the He-vacancy clustering process.

In an *in situ* TEM study (1×10^{16}/cm^2, from room temperature to 700 °C) [86], Frabboni *et al.* hypothesized that the void evolution starts with forming initial strain platelets by the clustering of the He atoms and the He_nV_m complexes in the damage regime below the size that would be visible in a TEM image. By examining *in situ* TEM images frame by frame, Frabboni *et al.* suggested that the cavity growth mechanism should be attributed to the migration and the coalescence of small bubbles in the temperature range of $360 \leq T \leq 570$ °C. Further increase in anneal temperature gives rise to continuous shrinking of small cavities with a corresponding growth of the central one in each individual cluster. Different from low temperature annealing, the authors proposed that Ostwald ripening (OR) should be responsible for the continuous shaping of the structures at high temperature (≥ 600 °C). This picture would imply that small cavities become unstable as the He outdiffuses and thus dissolve and annihilate with the large central void. Meanwhile, stress and dislocation loops start to decrease and eventually only a large single void in each cluster remains after prolonged annealing at temperatures close 700 °C. This proposal was supported by calculation of the total cavity volumes at different annealing stages, which indicate that there is only a very small variation in the total volume as the annealing temperatures rise.

Debate has continued regarding the actual mechanism by which coarsening takes place [88], [92]. The main arguments against and Ostwald ripening process are the symmetry of the planetary-like structures and the relatively constant volume during

thermal treatments. A migration and coalescence mechanism is more adequate to explain the void evolution process. This hypothesis is strongly confirmed by the observation of the effect of impurities on void nucleation. The incorporation of impurities such as oxygen, carbon, or nitrogen into the damage layer limits the bubble coarsening process [89], [90] [references therein]. This is due to the accumulation of impurity atoms on the cavity surface, which results in suppression of Si mobility on the surface and therefore, inhibits cavity diffusion and aggregation during annealing.

Finally, an interesting observation in terms of void size has been reported for HD and MD samples [83], [91]. It was found that the mean cavity diameter of MD samples is much larger than HD samples, following conventional furnace annealing. At annealing conditions of 800 °C for 10 minute periods, samples with implanted dose of 1×10^{16} cm^{-2} were found to have a d_m of 57 nm and a standard derivation of 9.5 nm, while for samples with implanted dose of 5×10^{16} cm^{-2}, a dense homogeneous array of bubbles with a d_m of 8.5 nm was detected [83]. Furthermore, the void size difference between HD and MD was also observed in samples with high implantation energy [91]. This seems to be related to the presence of dislocation loops surrounding the void bubbles in MD samples. In high energy studies [92], [93] the loops appear to emerge from clusters and the size and shape of the loop were found related to the cluster size, which indicates that the clusters are the loop sources. Any successful model of void formation should take these phenomena into account and properly include the role of strain.

Once these He bubbles are formed, increasing the annealing temperature and time results in He out-diffusion from bubbles. Under these conditions, typical Ostwald ripening clustering features have been observed in *in situ* TEM images as the effusion of

He atoms increases [86], [90]. The formation of central platelet-like cavity, which is due to the large He elastic free energy (or over pressurized He atoms), becomes unstable as He out-diffuses and the structure has to modify itself to a spherical shape in order to minimize the free energy [86].

4.3 Helium out-diffusion

The explanation of the dynamics of voids evolution is not complete without the consideration of out-diffusion of He. From the discussion presented in the previous section, the presence of He atoms in bubbles not only assists to stabilize open volume defects but it also enhances the bubble coalescing process in the intermedium dose regime. It has been emphasized that the He release rate during furnace annealing is almost half the rate when RTA annealing is performed on the same implant doses [85]. This explains why large voids were not found in the case of the RTA annealing ($d_m \sim$ 24nm) for MD implanted samples (1×10^{16} cm^{-2}) [96], even though the implantation conditions and the thermal treatment temperatures were the same as in the case of furnace annealing ($d_m \sim$ 57nm) [83]. In the following, a general description of He out-diffusion and the correlation between He effusion and void formation is given. Details on He effusion kinetics and modeling can be found by referring to [98].

It is well known that the He retained fraction strongly depends on the implantation depth. For implanted doses of 5×10^{16} cm^{-2}, 90% the He atoms were found to remain in cavities for samples with implantation energy of 1.6 MeV, while only 20% remained in the case of 40 keV implants, subsequent to the same annealing conditions

[94]. Indeed, Fichtner *et al.* [83] has demonstrated in a medium fluences (1×10^{16} cm^{-2}) study that the cavity's mean diameter d_m is doubled as the implantation energy increases from 10 keV to 40 keV. This reinforces the significance of the presence of over pressurized He atoms in the bubble aggregation process. Moreover, a recent investigation on the effect of the ramp rate on void formation has shown that the higher the He fraction retained in the LD samples, the larger and denser He_mV_n complexes in the damage region within a short annealing period [97].

Implantation and thermal treatment conditions, such as implantation doses/temperatures and annealing temperature/time, are the important factors that influence the He desorption rate during thermal treatments. Figure 4.1 shows the He out-diffusion rates for samples with implant doses in the range of 5×10^{15} cm^{-2} to 3.6×10^{16} cm^{-2} [82], [98]. In cases of low implanted fluences, the release of He starts at 250 °C and reaches the maximum peak in the interval between 350 to 400 °C. While in the medium fluences regime, a broad effusion peak centered around the temperature of 750 °C with a small shoulder peak at low temperatures is illustrated. Further increase in the implanted dose reduces the shoulder effusion peak and embeds into the high temperature board desorption region.

It has been suggested that the variation of He desorption profiles with respect to different implanted doses is due to the different bonding structure of He atoms in the cavities [82], [98], which reflects on the size of open volume defects. In general, the shoulder peak at low temperature is attributed to He out-diffusion from small and unstable He_nV_m complexes; whereas a much higher temperature is required to induce the out-diffusion from large cavities. Notice, a separation of the effusion profiles is clearly

shown for the implanted doses in the range of 8×10^{15} cm^{-2} to 2×10^{16} cm^{-2}. This implies that a more complicated void evolution process exists in this region, in which, the low and high temperature desorption peaks can be modified by the implantation and annealing conditions.

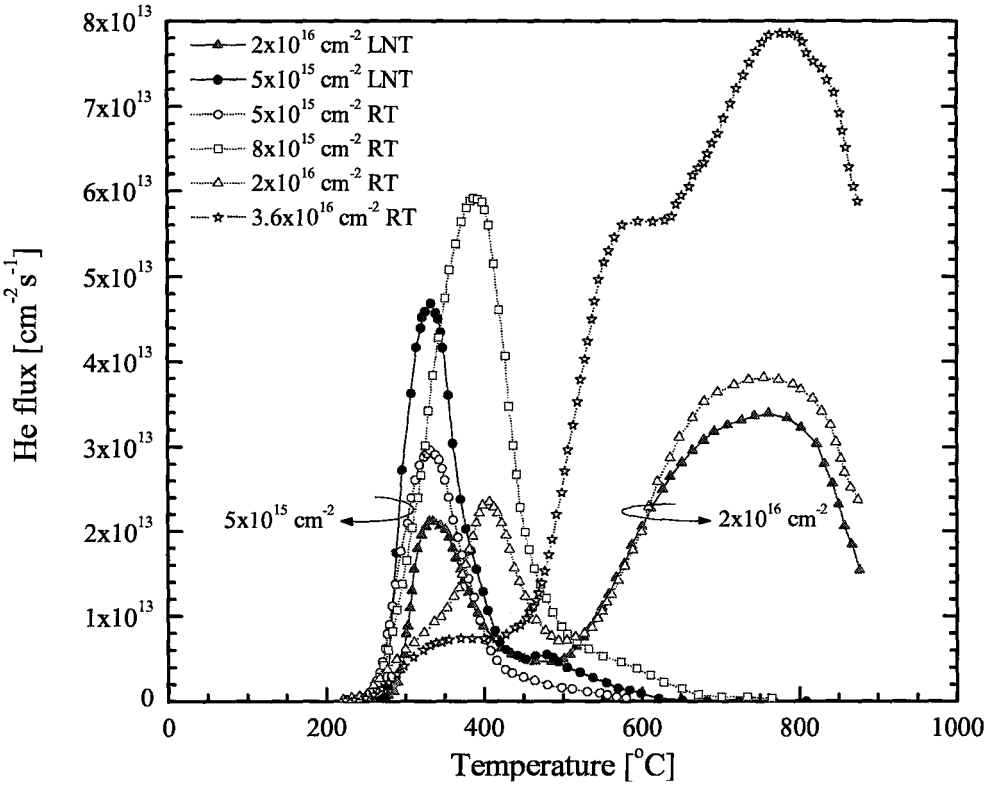

Figure 4.1. He desorption rates for various implanted samples at room temperature (RT) and liquid nitrogen temperature (LNT). The implantation energy and ramp up rate are 20 keV and 45°C/min respectively for all samples [82] [98].

It has been suggested that only samples with a broad He out-diffusion peak at 700 °C or higher will show voids in the cross-sectional TEM images after thermal treatment [99]. Nonetheless, subsequent to low temperature treatments, modification of the He effusion profile is possible. In Figure 4.2, reduction of the shoulder desorption peaks and strengthening of the broad peak is observed for samples with an implanted dose of 2×10^{16} cm^{-2} following two hours annealing at different temperatures [98]. Cerofolini *et al* [98]

suggested that low temperature pre-annealing destroys the He_nV_m complexes and that the He atoms from the destruction are mostly captured by the cavities. Therefore, it enhances the formation of stable voids in the subsequent thermal annealing. In conclusion, low temperature pre-annealing favors the void evolution for samples with low He implant doses.

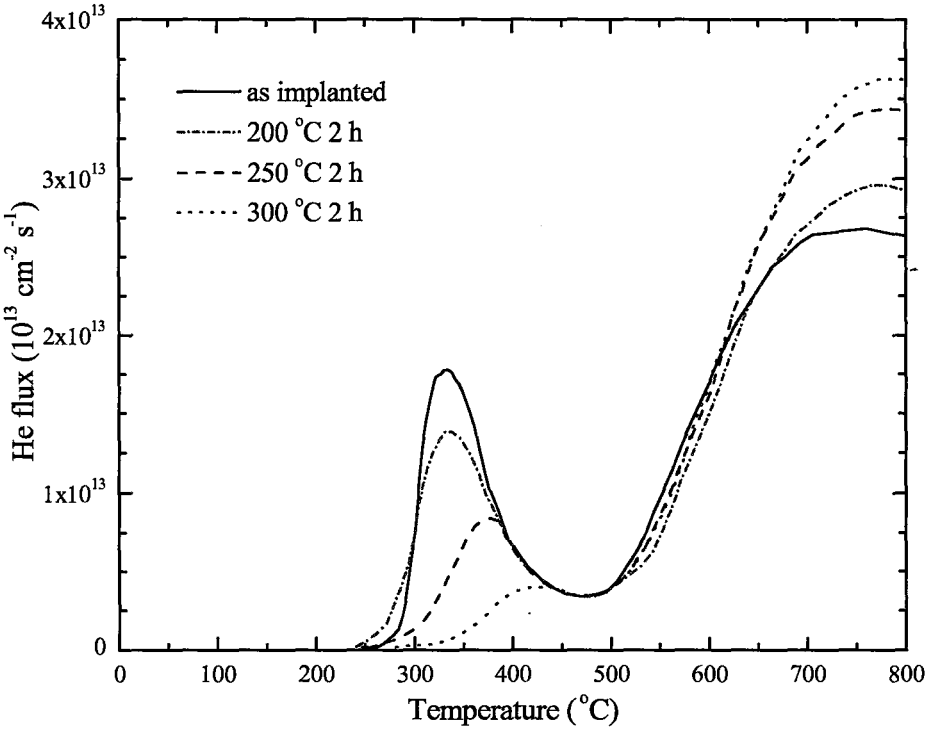

Figure 4.2. Thermal-desorption spectra from samples implanted at 2×10^{16} cm^{-2}, following isochronal annealing in temperatures between 200-300 °C. The samples were implanted at 20 keV and 77 K. The ramp up rate for thermal desorption was 45°C/min [98].

4.4 Effect of the implantation temperatures

Another important factor that affects the bubble formation is the implantation temperature, T_i. It is known that at temperatures above 150 K, radiation damage induced by ion implantation in silicon substrates can be significantly reduced by dynamic

annealing, which is the *in situ* recombination of interstitials and vacancies during implantation. The self-annihilation determines the amount of vacancies that exist in the damage layer after the implantation, which in turn affects the driving force toward cluster formation and growth. Recent studies [96], [100], [101] show that void formation follows a distinct microstructure evolution route at different implantation temperatures due to the changes in the target temperatures strongly influences the formation of He_nV_m complexes and the outdiffusion of He gas.

For large implanted fluences, the variation of implantation temperature has a relatively small effect of the voids formation, in terms of size and density. However, as the implant dose decreases, a larger impact is clearly observed [96]. In the implant dose of $1\times10^{16}/cm^2$, *s*ubsequent to high temperature anneal, cavity's mean radius (r_m) increases as implantation temperature decreases from room temperature (RT) to liquid nitrogen temperature (LNT), while the density of the cavities decreases [96]. This has been attributed to the limited amount of dynamic annealing at the LNT temperatures, which gives rise to abundant vacancies that interact with the trapped He atoms. Upon thermal annealing at higher temperatures, a relatively large quantity of cavities with different sizes randomly distributed in the implanted layer is observed. While for RT implantation, a diluted system of planetary structure is obtained. Further increase in the implantation temperature results in an array of small unstable bubbles form in the as-implanted state, which might completely annihilated following high temperature treatment.

4.5 Summary

A detailed examination of voids formation in silicon substrate under ion implantation of He was given in this chapter. The He implanted dose is the key parameter that determines the void evolution and modification process during high temperature treatments. In particular, large voids are not formed for an implant dose below 10^{16} cm^{-2}. For doses significantly above this threshold, a uniform damage layer forms with voids of a uniform size. At intermediate implant doses, the density of voids in the material is significantly lower and they take the shape of a large central cavity surrounded by smaller satellite cavities. In all cases the thermal annealing profile is critical in determining whether voids form in the manner just described or whether they dissociate into point defects that are then annihilated via diffusion to the surface. In addition to the anneal temperature and time, it also appears that ramp rates may have a critical effect on void formation as evidenced by the difference between RTA and furnace results. In all cases, the formation of voids appears to proceed via formation of He-V clusters followed by the outdiffusion of He to leave behind the voids. Some modeling of this process has been attempted in the literature but much more is required. Finally, the implant temperature is also an important factor in the formation and growth of these voids. The effect of implant temperature is tied to the phenomenon of dynamic annealing that allows implant damage to anneal *in situ* if the implant temperature is sufficiently high.

In the next two chapters we describe our own experiments and results where we investigated the impact of the annealing thermal profile on void formation after medium dose implants.

Chapter 5

Experiment Technique and Preparation

This chapter provides an overview of our experiments to investigate void formation and vacancy injection in Si and SiGe. We have relied heavily on positron annihilation spectroscopy (PAS) in the measurement of vacancies and voids. Section 5.1 introduces this technique in some detail. Section 5.2 is a detailed description of our experiments, and Section 5.3 describes our efforts to calibrate the furnace used in our thermal anneals to allow a reliable analysis of the data as to the effect of the thermal profile of the anneals.

5.1 Positron annihilation spectroscopy

The positron is the antiparticle of an electron, meaning it has the same physical properties, but with a positive charge. It has been discovered that when a high-energy positron impinges upon a sample surface, it rapidly slows down within picoseconds by the interactions and collisions with ionized atoms, nuclei, and phonons, until thermal equilibrium is achieved with the surroundings. At this point the positron diffuses through the lattice until it is trapped in a defect site or annihilated with an electron. The trapping of a positron most commonly occurs in the presence of open volume defects, such as vacancies, clusters or voids. This is because of the nonexistence of repulsive positively charged nuclei in the aforementioned defects. The lifetime of a positron trapped in such large open volumes is increased due to inherently lower electron density.

Utilizing the enormous sensitivity of positrons to vacancy defects and the γ-radiation produced during annihilation, Positron Annihilation Spectroscopy (PAS) has been developed since the late 1960s to detect imperfections in crystalline materials. The differences in electron density and the electron momentum distribution in defects, as compared to that of perfect crystalline structures, result in a different γ-radiation emission in the annihilation process, hence strongly reflecting the local defect environment. Vacancy concentration as low as 10^{15}~10^{19} cm^{-3} can be detected by PAS [102]. Neutral and negatively charged vacancies are the positron dominant traps in semiconductors. The repulsion between positrons and positively charged vacancies prevents them from acting as traps and renders them "invisible" to PAS.

5.1.1 Positron sources

High-energy linear accelerator (LINAC) pair production and the radioactive decay of a nucleus are the two most commonly used techniques to produce positrons. In high-energy linear accelerator pair production, photons (γ rays) are emitted by the Bremsstrahlung process as highly energized electrons are stopped in a dense high atomic number absorber such as Tantalum. When the photon energy is more than twice that of the electron rest mass energy, a neutron can be ejected from a parent nucleus, leaving the nucleus proton-rich and unstable. To return to a stable configuration, the excess proton decays into a positron (β^+) and an electron neutrino (ν_e). In addition, electrons are produced simultaneously with positrons by the pair conversion of these photons. Because of the requirement of a dedicated laboratory facility and appropriate electron accelerator, this technique is not widely used.

The second, more regularly used method is providing the positron source via the radioactive decay of radio-isotopes such as ^{22}Na, ^{64}Cu and ^{58}Co. ^{22}Na has a long half-life time of 2.6 years (as compared to 12.8 hrs and 71 days for ^{64}Cu and ^{58}Co respectively), can be obtained from easily handled source materials (sodium chloride or sodium acetate), and is available at reasonable prices, all qualities which make ^{22}Na the most popular isotope source for positron research. Moreover, ^{22}Na has a much higher positron branching ratio of 0.904, as compared to 0.15 in ^{58}Co. By definition, the positron branching ratio is the number of positron emissions over the total number of decay emissions. In this work, positrons were obtained by the decay of radioactive isotope ^{22}Na following the reaction equation:

$$^{22}Na \rightarrow {}^{22}Ne + \beta^{+} + \nu_e + \gamma \tag{5.1}$$

The rapid decay of ^{22}Na reaches the excited state of ^{22}Ne by generating a high percentage of positrons (β^{+}) and a relatively small amount of electron capture (EC). Following the positron emission, a γ-quantum with energy of 1.27 MeV is produced almost simultaneously within 3.7 psec, after which the ground state of Ne is reached. A simple decay scheme of the radioactive isotope ^{22}Na is illustrated in Figure 5.1.

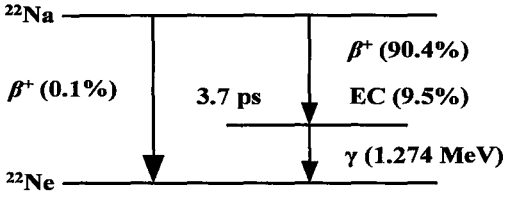

Figure 5.1. 90.4% of the radioactive isotope ^{22}Na decay results in emission of positron and an electron neutrino. A γ-quantum with energy of 1.274 MeV is emitted followed by the positron generation. Direct transition to reach the ground state of Ne and the electron capture also occur at lower probabilities [103].

5.1.2 Basic positron annihilation processes

The mass-energy transformation of electron-positron annihilation leads to the emission of two γ-quanta in opposite directions, each with an exact energy of 511 keV. This annihilation radiation strongly reflects the electron density and electron momentum distribution, hence the defect information at the annihilation site. In principle, positron spectroscopy analysis can be classified into two techniques: Positron Lifetime Spectroscopy (PLS) and Doppler-Broadening Spectroscopy (DOBS). A schematic illustration of the two methods is shown in Figure 5.2. The emission of the 1.27 MeV birth γ-quantum is produced nearly simultaneously with the positron beam by the decay of radioactive isotope ^{22}Na. This allows for the direct measurement of the positron lifetime Δt by extracting the time difference between the birth (1.27 MeV) and annihilation (511 keV) γ-quanta. Furthermore, the propagation component of the annihilation γ-ray causes an angular deviation from 180° between the two 511 keV radiations resulting in a Doppler shift in their energy. Many other positron measurement methods have been also developed in the past, including angular correlation of annihilation radiation (ACAR), low energy positron diffraction (LEPD), and age-momentum correlation. However, the examination of vacancy defects in this study was conducted by Doppler-Broadening Spectroscopy, therefore, only the DOBS technique will be given in detail. Because of its particular importance, we also include a brief introduction to Positron Lifetime Spectroscopy is also included.

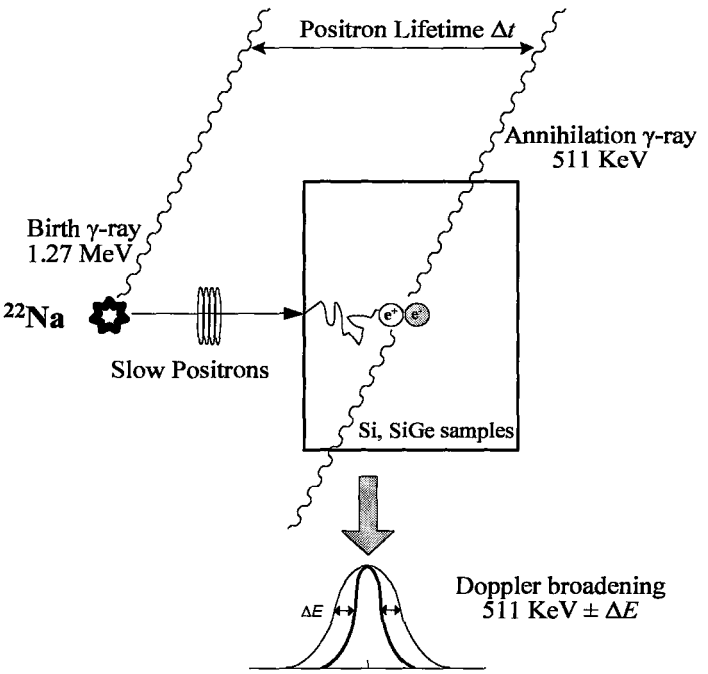

Figure 5.2. The two principle positron spectroscopy techniques: Positron Lifetime Spectroscopy and Doppler Broadening Spectroscopy. The positron source is generated by the decay of the radioactive isotope, ^{22}Na. A slow positron moderator is used for the shallow surface depth analysis. Positrons are thermalized within a few psec and diffuse before trapping or annihilation.

5.1.3 Thermalization and diffusion of positrons

A broad positron energy distribution up to 540 keV can be obtained from the radioactive decay of ^{22}Na, which allows for deep positron penetration, up to hundreds of microns into the sample substrate. This penetration process occurs very rapidly within the period of a couple of picoseconds as the positron is thermalized with the surroundings. According to the implantion energy, the penetration profile ψ (at a depth x) can be described as:

$$\psi(x) = \exp(-\alpha x), \tag{5.2}$$

$$\textit{with} \qquad \alpha = 2.8\frac{\rho q^{0.15}}{\overline{E}^{1.99}}[\mathrm{cm}^{-1}] \tag{5.3}$$

where α is the positron absorption coefficient for ^{22}Na [104], ρ is the mass density of the substrate material, q is the average atomic number and $\overline{E}$ is the mean positron energy which is 0.15 MeV for ^{22}Na.

Because of the extremely high implantation energy, positron thermalization usually consists of three stages: mass radiative stopping (Bremsstrahlung), electron scattering and phonon interaction [105]. For energies in the order of hundreds of keV, photons are emitted through the Bremsstrahlung process as positrons interact with atomic orbital electrons. This reduces the energy level to as low as ~ 100 keV. In the electron scattering stage, positron energy further decreases by inner shell ionization and electron-hole pair generation. In the last step, since positron energy might have already fallen below the band gap energy, phonon interaction completes the positron thermalization process. Nonetheless, depending on the atomic number of the substrate material and positronium (e^+-e^-) formed at the sample surface, a fraction of positron reaches the surface and escape from the sample if the positron energy is larger than the positron work function.

Due to the repulsion with nuclei, positrons spend most of their time in interstitial regions after the thermalization process as they further diffuse within the crystal. The typical positron diffusion coefficient at room temperature (300 K) is in the range of 1.5-3 cm^2s^{-1} [106]. Consequently, a large diffusion distance (~100 nm) can be achieved within a very short period as compared to positron lifetime. This means that a positron can "scan" through a considerably large volume in search for defects before it annihilated with electron.

Regardless of the diffusion length of positrons, studies on point defects in semiconductors are mainly concerned with depths on the order of a few to hundreds of nanometers. Thus modification of the positron energy is necessary in order to achieve the small penetration depth typically required. Moderation is often used to obtain monoenergetic positrons or slow positron, Figure 5.2. Only a small fraction (<1%) of incident positrons go through the moderation process. The un-moderated positrons must be separated from the monoenergetic positrons by either utilizing a beam magnetically guided system or by completely stopping using bent solenoids [103].

5.1.4 Positron lifetime spectroscopy

The lifetime of positrons, Δt, depends on the electron density at the annihilation site. This permits the formulation of the positron lifetime as a function of the electron density and its reciprocal gives the total positron annihilation rate λ.

$$\lambda = \frac{1}{\Delta t} = \pi r_o^2 c \int \left|\psi^+(r_p)\right|^2 n\_(r_p)\chi dr \tag{5.4}$$

r_o is the classical electron radius, c is the speed of light, $|\psi^+(r_p)|^2$ and $n\_(r_p)$ are the positron and electron densities respectively. The correlation factor χ and the positron vector r_p are also included in the equation. The positron wave function in solid matter [106] differs in accordance to the different structures the positrons encounter, such as perfect crystal, monovacancy, divacancy or voids. The positron lifetime in these structures varies such that the larger the cavity size, the longer the lifetime due to the lower electron density. In defect free bulk substrates, the positron lifetime Δt_B is relatively small as compared to the one that is defect related Δt_D. It has been reported that the experimental

bulk lifetime for Si is 218 ps and Ge is 228 ps [103]. Utilizing Δt_B as a reference, the vacancy defect size can be determined by evaluating the $\Delta t_D/\Delta t_B$ ratio. A ratio value close to 1.2 indicates the existence of mono-vacancies, while a ratio of 1.4 shows the formation of divacancies and a much larger ratio value can account for vacancy agglomerates or voids. A defect-related positron lifetime versus the vacancy size of neutral vacancy clusters in silicon is given in Figure 5.3.

While the positron lifetime ratio reflects the vacancy cluster size, the positron trapping rate k_p shows the cluster concentration V_c through the equation

$$k_p = \Gamma V_c, \tag{5.5}$$

where Γ is the trapping coefficient. The trapping rate k_p changes according to different type of defects and can be calculated from the corresponding lifetime Δt and intensities I_p from the lifetime spectrum. To further understand the technique, the reader may refer to the references [103] - [107].

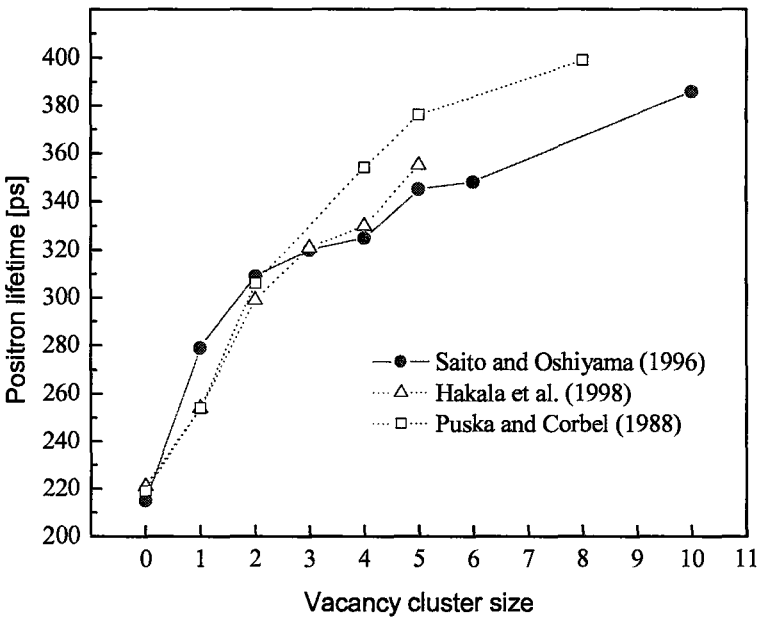

Figure 5.3. Illustration of *ab initio* calculation of positron lifetime versus neutral vacancy cluster size. The bulk lifetime corresponds to 0 vacancies. Dashed and solid lines indicate the lifetime for ideal and relaxed geometries, respectively [103].

5.1.5 Doppler broadening spectroscopy

During the positron annihilation process, the two resultant 511 keV γ-rays do not radiate exactly 180° from each other. This phenomenon occurs because the momentum conservation of electron-positron pairs is dominated by the electron motion due to the significantly smaller momentum of positrons after thermalization. Consequently, the momentum component of the electron-positron pair yields a Doppler shifted and angular deviated γ radiation corresponding to the electron distribution at the annihilation site. The Doppler shift may be approximated by

$$\Delta E = \pm P_z \frac{c}{2} \tag{5.6}$$

where P_z is the momentum component along the γ-ray propagation direction and c is the speed of light. Typical Doppler-broadening spectra of perfect crystal and defect rich semiconductors are given in Figure 5.4. In a perfect crystal, the Doppler-broadening spectrum consists of a narrow peak that corresponds to the annihilation with conduction electrons and broadening at the two extremes that arises from annihilation with core electrons. As positrons become localized in open-volume defects, the probability of their annihilation with valence electrons increases as compared to that of core electrons. This results in a smaller Doppler shift because of the considerably lower momentum of valence electrons. Thus the curve of a defect-rich semiconductor is higher and narrower than that of defect-free reference, when both curves are normalized to equal area.

Doppler broadening spectra can be easily distorted by background events if the signal is recorded from only one of the γ-rays, making it difficult to calculate the Doppler broadening parameters. By utilizing two detectors for the simultaneous detection of both γ-rays, the energy resolution increases by a factor of $\sqrt{2}$ [108]. This method, called the

Doppler-broadening coincidence technique, was first developed by Lynn *et al.* [109] in 1977 and is illustrated in Figure 5.5. High-resolution energy-dispersive liquid nitrogen cooled germanium detectors are used to measure the broadening of the annihilation spectra. The photon radiation energy is converted to an electrical signal by a pair of preamplifiers and then followed by analog-to-digital conversion (ADC) and subsequent digital processing in the multi-channel analyzer (MCA). It should be noted that the γ-ray energy recorded by the two detectors will in general be different. If detector A receives a γ-ray energy higher than 511 keV then a corresponding decrease would simultaneously be found by detector B. However, the total annihilation radiation energy remains constant at 1022 keV.

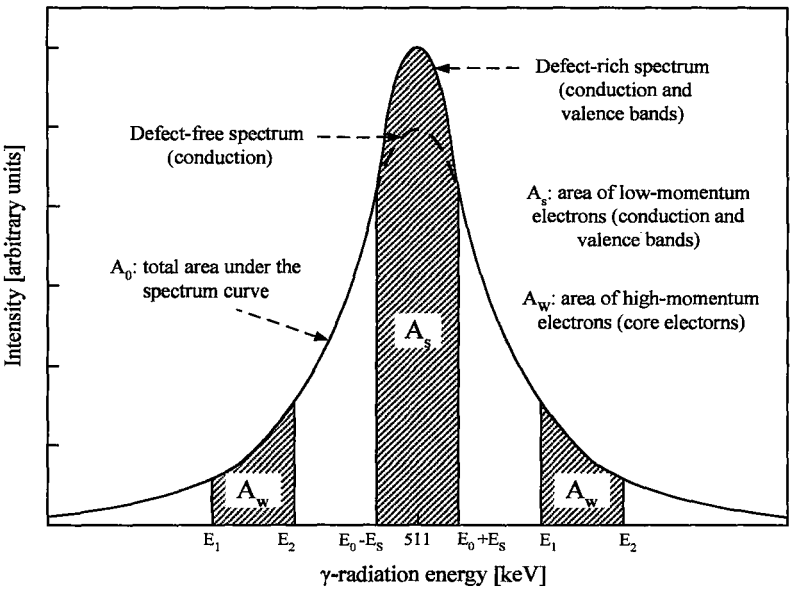

Figure 5.4. Illustration of Doppler-broadening spectrum of both perfect crystal and defect rich (vacancies) semiconductor material. E_0 is the central energy which equal to 511 keV. E_S is the chosen parameter that to calculate the counts in the low-momentum region (A_S). E_1 and E_2 are the chosen parameters for high-momentum window (A_W). The curves are normalized to equal area.

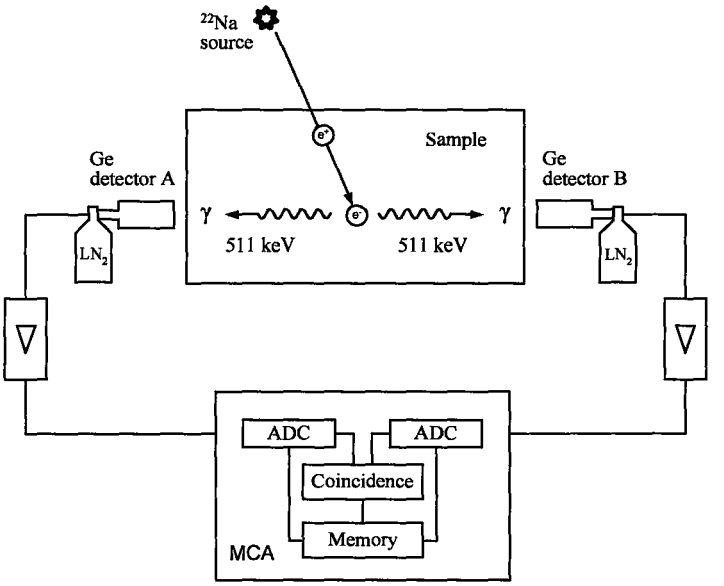

Figure 5.5. A simple schematic demonstration of the Doppler-broadening coincidence technique. The background is suppressed by the simultaneously recording of the two γ-rays using high efficiency Ge detectors.

Regardless of the significant advantages of the coincidence technique in the Doppler-broadening spectroscope as compared to the single detector method, the conventional single Ge-detector is the dominant detection method when it comes to measuring *V* type defects. This is because of the large time consumption attributed to the coincidence technique, in which one spectrum may take up to 24 hours to accumulate, while for the single detector method, only a few minutes is required. In addition, it is believed that a single detector can reliably distinguish the type of *V* defects, divacancies or voids [110].

To obtain a clearer picture of the Doppler-broadening spectrum due to positron trapping in open-volume defects, specific line shape parameters are developed to quantitatively evaluate the spectra. The *S*-parameter (for Shape) is defined as the ratio between the counts in the low momentum region (i.e. central area A_S) to the total counts

under the spectrum curve (i.e. area A_0), and the W-parameter (for Wing) is defined as the ratio of counts in the high momentum region (i.e. window area A_W) to the total count A_0.

$$S = \frac{A_S}{A_0},\ A_S = \int_{E_0-E_S}^{E_0+E_S} N_D dE \tag{5.7}$$

$$W = \frac{A_W}{A_0},\ A_W = \int_{E_1}^{E_2} N_D dE \tag{5.8}$$

where $N_D = f(E)$ is the function of number of counts at a particular energy. To get useful information out of these parameters, proper choice of energy windows is important. The central interval of the low-momentum case should be chosen to be symmetrical around the energy of E_0 = 511 keV, and such that area A_S covers about 50% of the total area for defect-free material ($S \sim 0.5$). An increase in the S-parameter value corresponds to increases in vacancy-like defect size and density. For the high-momentum case, the interval selected needs to be far enough from the central region to ensure that only core annihilations are considered. Thus the energy limits E_1 and E_2 must be defined in such a way as to have no correlation effects with the S-parameter.

5.2 Experiments

Two types of substrates were used in this work: Float-Zone (FZ) grown {100} orientation silicon wafer with resistivity of 8000 – 10000 Ω·cm and undoped Czochralski (Cz) grown {100} orientation SiGe wafer with approximately 8 percent Ge content. All substrates were implanted with He^+ at a dose of $1\times10^{16}/cm^2$ and energy of 60 keV with a beam current density of ~ 10 μA cm^{-2}. The sample temperature during implantation was maintained at room temperature (300 k) and the sample holder was tilted at 7° with

respect to the normal of the beam to minimize channeling effects. The implantation was done in the University of Western Ontario. Figure 5.6 shows the helium and vacancies depth-concentration profiles in the silicon samples obtained by a Stopping and Ranges of Ions in Matter (SRIM) simulation [111] of the as-implanted state, where the He projected range, R_p, is 472 nm with straggle ΔR_p of 108.6 nm. In the implanted region between 450 to 550 nm, the He concentration is well above the critical dose required for the formation of visible voids under TEM measurement [3.5 (±1) $\times 10^{20}$ cm^{-3}]. A shift in the vacancies profile with respected to that of He is also observed in the figure. Note that, the consideration of the *in situ* self-annihilation effect during implantation is not included in the SRIM calculation.

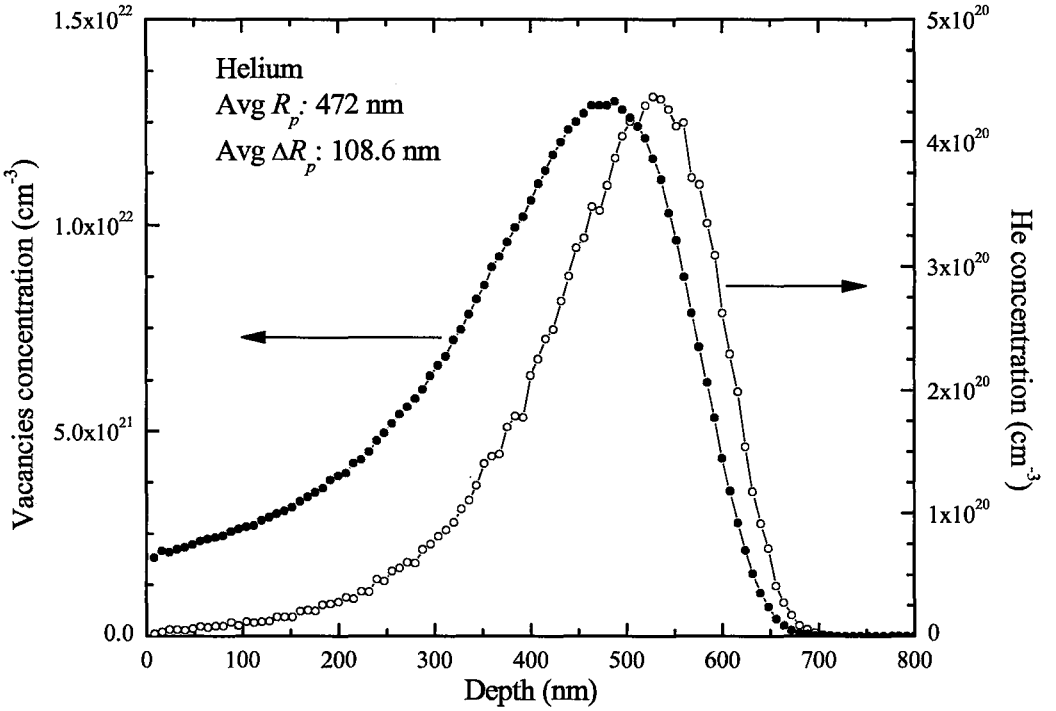

Figure 5.6. He and vacancies depth-concentration profiles in Si substrate calculated by the SRIM code [111].

Table 1. Summary of annealing conditions for voids formation in silicon samples. Samples a, b and c were annealed in inert ambient (N_2), while d, e and f were annealed in oxygen ambient (O_2).

Sample	Annealing Temperature	Ramp up rate	Annealing Time (min)
1 a, d	700 °C	100 °C/sec	1
1 b, e	700 °C	100 °C/sec	10
1 c, f	700 °C	100 °C/sec	30
2 a, d	800 °C	100 °C/sec	1
2 b, e	800 °C	100 °C/sec	10
2 c, f	800 °C	100 °C/sec	30
3 a, d	1000 °C	100 °C/sec	1
3 b, e	1000 °C	100 °C/sec	10
3 c, f	1000 °C	100 °C/sec	30
4 a	600 °C	50 °C/sec	10
4 b	600 °C	100 °C/sec	10
4 c	600 °C	200 °C/sec	10
5 a	700 °C	50 °C/sec	10
5 b	700 °C	100 °C/sec	10
5 c	700 °C	200 °C/sec	10
6 a	800 °C	50 °C/sec	10
6 b	800 °C	100 °C/sec	10
6 c	800 °C	200 °C/sec	10
7 a	900 °C	50 °C/sec	10
7 b	900 °C	100 °C/sec	10
7 c	900 °C	200 °C/sec	10

After the implantations, samples were cleaned by a dilute HF dip followed by a DI water rinse. For the void formation study, Si samples were rapid thermal annealed in inert (N_2) or oxygen (O_2) ambient in the temperature range of 600 °C to 1000 °C for different time lengths and ramp up rates. The annealing pressure and gas flow rate were kept at atmosphere pressure and at 500 SCCM, respectively. Some of the annealing was done at the University of Western Ontario and the rest was done at McMaster University. Table 1 shows the annealing conditions for all of the Si samples.

To identify the type of defect that is being injected during wet oxidation of SiGe, voids were formed in two $Si_{0.92}Ge_{0.08}$ samples (A and B) by He implantion before the oxidation process. After the implantation, both samples were HF cleaned and annealed at

800 °C for 10 minutes in an RTA nitrogen ambient, where the gas flow rate and pressure were 500 SCCM and 1 atm, respectively. The ramp up rate was 100 °C/sec. To our knowledge, this is the first study involving He implants to form voids in a SiGe substrate. However, due to the similarities between Si and Ge, the voids formation and evolution process in the $Si_{0.92}Ge_{0.08}$ sample is expected to be analogous to the case of Si.

Void formation in the SiGe samples was confirmed by PAS analysis following the 10 minute thermal treatment. Samples were then HF cleaned before further heat treatments. For the wet furnace oxidation, pure oxygen was bubbled through DI water at a temperature of 95 °C with a flow rate of ~ 1 SLM. The furnace temperature was set to be 850 °C at atmospheric pressure. When the temperature reached a steady state, sample A was slid into the furnace with an approximate ramp up rate of 160 °C/sec. The oxidation was performed for 30 minutes. To capture the phenomenon of void self-annihilation under high temperature, an inert nitrogen anneal was preformed on sample B in the same furnace. The annealing was done with the same temperature, flow rate and time length. Quantitative positron analysis was performed on the two samples to show any change in the void size. Comparison of the two sample indicates the corresponding type of defect injected during oxidation (no defects are injected during the inert anneal and this sample serves as a reference to demonstrate the rate of void dissolution without any defect injection).

All defect measurements utilized the single Ge–detector Doppler-broadening technique as described earlier in this chapter. For the Si samples in the void formation study, positron analysis was done at the University of Western Ontario while for the oxidation study, the analysis was done at the University of Bath in the United Kingdom.

5.3 Furnace calibrations

One of the major concerns with annealing experiments is the setup of the equipment. Specifically, we are concerned about temperature uniformity and stability, and with maintaining laminar flow for process gases. To verify the accuracy of the furnace and RTA machine, we have conducted wet and dry silicon oxidation in the two stations, respectively. All annealings were performed at 800 °C and 900 °C using the settings described above. For the wet furnace oxidation, P-type boron doped Si samples with {100} orientation and resistivity of less than 1 Ω·cm were used. It was found that temperature variation over the length of the furnace tube leads to a systematic variation in oxide thickness and turbulent gas flow leads to islanding and/or non-uniform film thickness. By readjusting the flow rate, visual inspection reveals no islanding, and measurement of the index of refraction shows a good quality oxide across the entire sample. Thermocouple measurements show a systematic temperature variation along the length of the tube of ~ 5 °C/cm at the gas flow rate of 1 SLM. Oxide thickness difference across the sample correlates well with this variation, resulting in a change of ~ 3 nm/cm for a 1 hour oxidation. By comparing the oxide thicknesses with simulation results obtained using the Deal and Grove model [44], the furnace temperatures are off by 40 °C to 50 °C, within the calibration ranges. Thus the actual annealing temperature in our SiGe oxidation study should be 890 to 900 °C, since the furnace setting point was 850 °C.

FZ silicon substrates as described before were used in the dry oxidation calibrations. The settings of the RTA machine were the same as that used in the He^+ implanted voids formation study. The anneals were carried out at 800, 850 and 900 °C for the periods of 1 and 3 hours. The experimental data and the simulation values for the dry

oxidation at different annealing conditions are plotted in Figure 5.7. A large thickness variation between the two indicates that the actual temperature inside the chamber is significantly higher than the thermocouple reading. Furthermore, the difference is systematic, changing according to the annealing temperatures and time lengths, where lower annealing temperatures and shorter annealing periods lead to larger variations. This can be seen by comparing the simulation and experimental results in Table 2 and Table 3. The unstable RTA annealing conditions explains the abnormal results obtained in samples 4 to 7 in the voids formation study.

In the following chapter, the significance of the experimental results of void formation under various annealing conditions and defect generation during wet oxidation of SiGe are discussed.

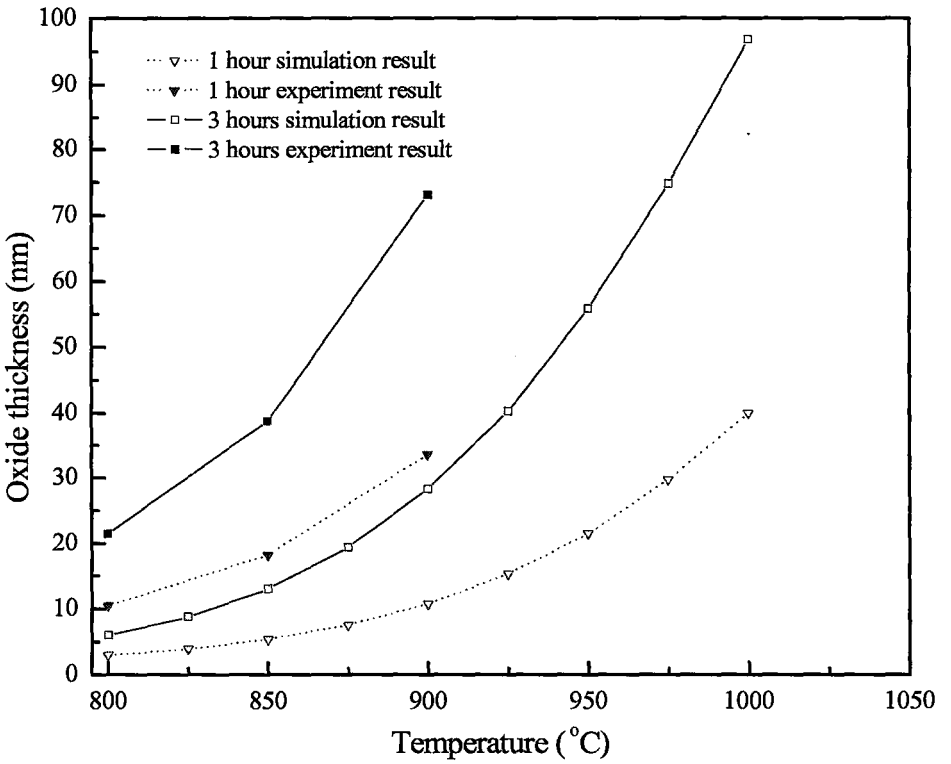

Figure 5.7. RTA calibrations - oxide thicknesses vs. temperatures. Simulation values obtained from D & G model.

Table 2. Simulation and experimental results of oxide thicknesses and temperatures for 1 hour oxidation. Native oxide was assumed to be 1.5 nm

D & G Simulation Value		Experimental Value		Off by
Temperature	Oxide thickness	Temperature	Oxide thickness	
897 °C	10.32 nm	800 °C	10.498 nm	97 °C
940 °C	18.775 nm	850 °C	18.1943 nm	90 °C
985 °C	33.5 nm	900 °C	33.563 nm	85 °C

Table 3. Simulation and experimental results of oxide thicknesses and temperatures for 3 hour oxidation. Native oxide was assumed to be 1.5 nm

D & G Simulation Value		Experimental Value		Off by
Temperature	Oxide thickness	Temperature	Oxide thickness	
881 °C	21.2 nm	800 °C	21.45 nm	81 °C
922 °C	38.638 nm	850 °C	38.758 nm	72 °C
973 °C	73.109 nm	900 °C	73.053 nm	73 °C

Chapter 6

Results and Discussions

6.1 Voids formation

6.1.1 The effect of annealing temperatures and times

The positron measurements for the Si samples of void formation under inert nitrogen anneal are given in Figure 6.1. To obtain meaningful quantitative data, the *S*-parameters were normalized to the bulk value and the mean positron annihilation depths (Z) were converted from the probing energy following the relationship of

$$Z = \left(33/D_S\right)E^{1.6} \text{ nm}, \tag{6.1}$$

where D_S is the sample density (g.cm^{-3}) and E is the positron implantation energy in keV [114]. Despite the small uncertainty induced by the Doppler broadening single detector technique, due to the presence of background events as was discussed in the pervious chapter, it is generally believed that the normalized *S*-parameters obtained using this method can reliably distinguish different types of V-defects. As such, an *S*-parameter in the range of 1.04 – 1.06 is considered to be indicative of di-vacancies and vacancy-impurity complexes, and when in the range of 1.06 – 1.15 larger vacancy clusters, or voids, are believed to be present in the substrate [110]. In this study, sizes of open volume defects are approximated by fitting the positron data to a linear relationship of *S*-parameters and cavity diameters.

As shown in Figure 6.1, relatively large voids were only observed in the cases of annealing temperatures of 700 and 800 °C and void formation is almost entirely inhibited

as the anneal temperature is increased to 1000 °C. This major difference is believed to be caused by the rapid out-diffusion of He and the fast annihilation of V-type defects with displaced Si atoms at such high temperatures. To have a better idea of the size of the voids, TEM measurements were preformed on sample 2b (800 °C for 10 minutes). Similar to those reported in the literature [86], a layer of diluted planetary-like structures in the damaged region is observed in the low magnification TEM image, Figure 6.2 (a). The dark fields in the vicinity of the layer indicate significant strains developed during the bubbles evolution process and that it is the result of trap-mutation of the over-pressurized He atoms inside the bubbles (section 4.2). A high resolution TEM image of a typical void in the layer is given in Figure 6.2 (b). The strong strain field surrounding the void further signatures of loop punching mechanism and the Si atoms ejected from the cavity surface to release the high pressure during the process.

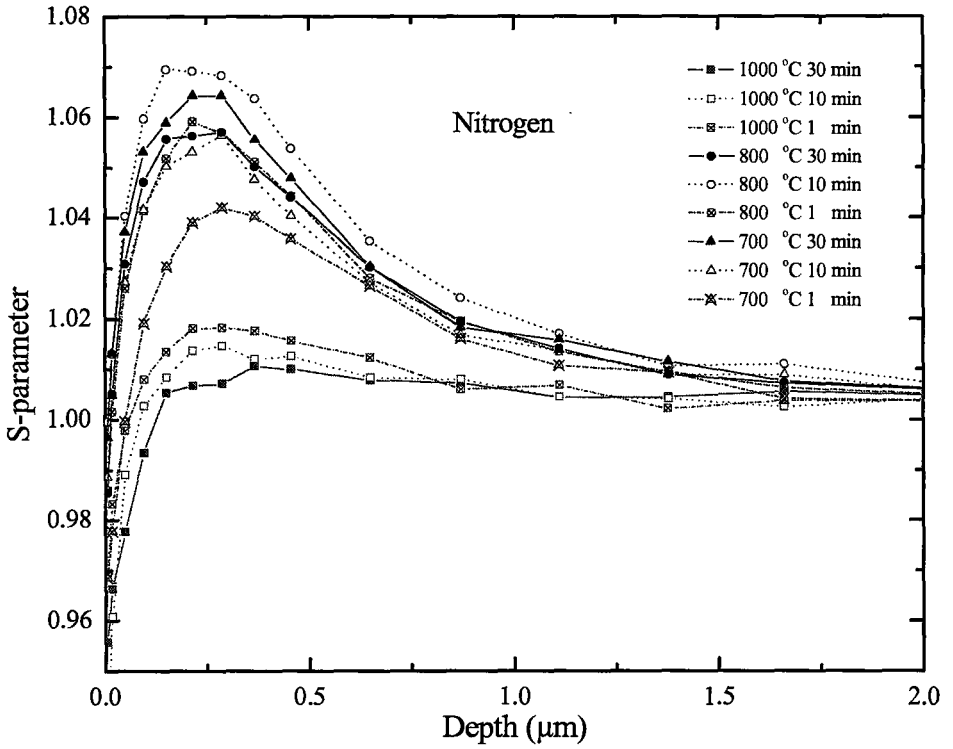

Figure 6.1. Normalized S-parameters vs. positron probed depth for samples 1a, 1b, 1c, 2a, 2b, 2c, 3a, 3b, and 3c. All samples were annealed in nitrogen RTA ambient for different time lengths and temperatures.

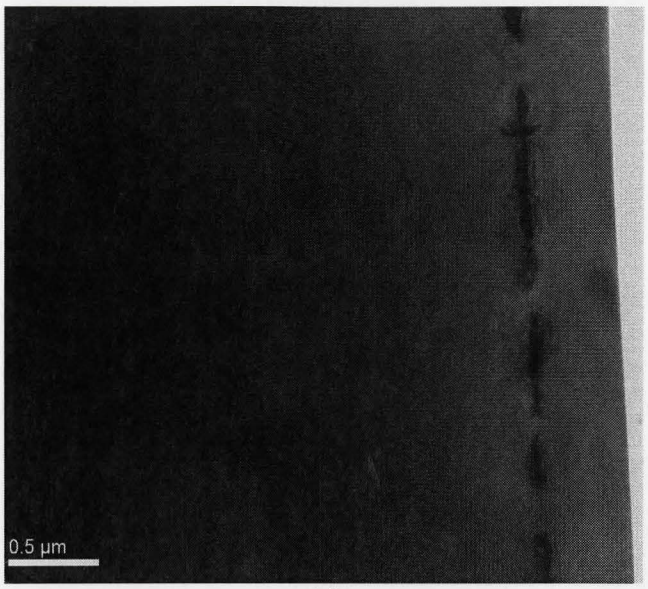

(a)

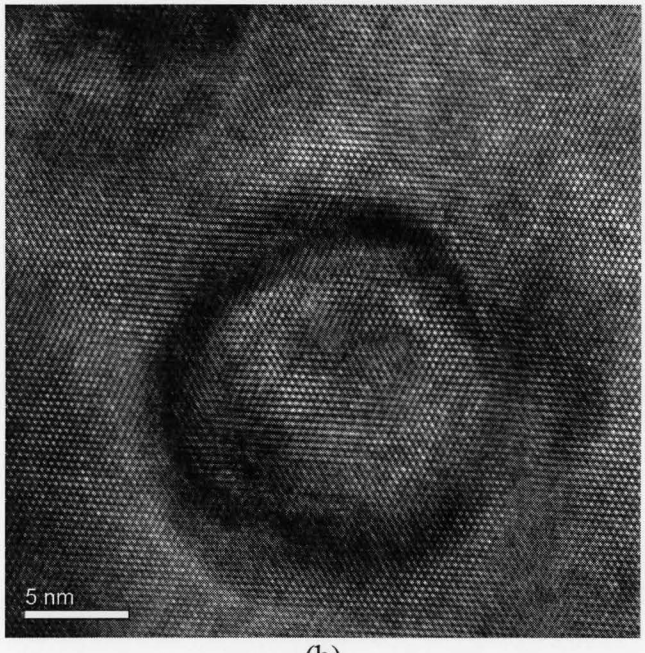

(b)

Figure 6.2. TEM images of a typical void in sample 2b, nitrogen RTA for 10 min at 800 °C: (a) cross section images of a layer of voids in the implanted region and (b) plan view high resolution image of a typical void with diameter of 15 nm.

In order to correlate the *S*-parameters that were obtained from the other samples to a physical cavity size, a quantitative fitting equation has been developed. By assuming that the void's diameter is zero when the normalized *S*-parameter is equal to one and that

the diameter of 15 nm is equivalent to the *S*-parameter of 1.069, as seen for sample 2b in Figure 6.1 and Figure 6.2 (b), a linear relationship of the cavity size as the function of *S*-parameter is created. The approximated void sizes for samples annealed in N_2 ambient are given in Figure 6.3. Different growth patterns associated with a specific annealing temperature may be determined. At 1000 °C, cavities shrink as the annealing time increases as is shown in the figure. For lower temperatures, such as 700 °C, the continuous coarsening of small bubbles within the annealing period is observed. While for the 800 °C case, the maximum cavity volume is found after 10 minutes of treatment, which is then followed by a gradual decrease of void diameter with a prolonged anneal. These different evolution behaviors are believed to have a strong correlation with the out diffusion of He gas, which will be discussed as follows.

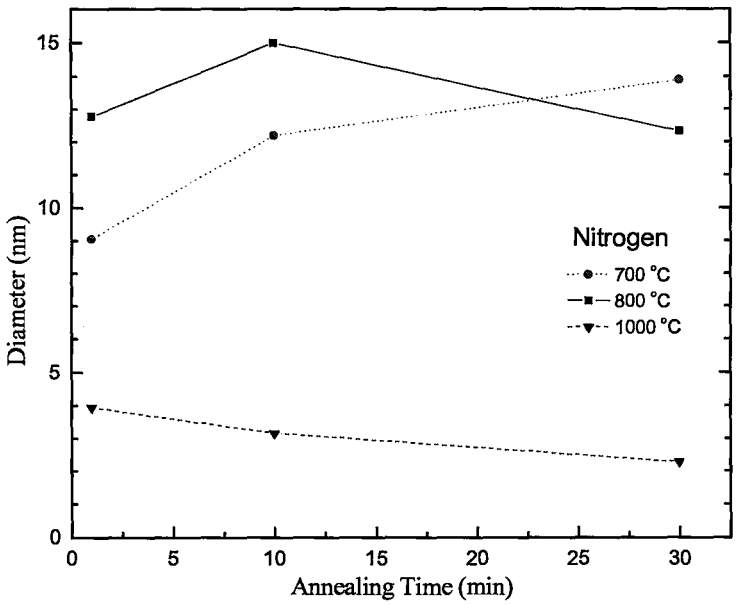

Figure 6.3. Rough estimation of void's diameter vs. annealing time for the samples annealed in N_2 ambient.

Despite the inaccuracy introduced by the rough cavity size approximation, there is no doubt of the growth/shrinkage evolution pattern in each of the annealing temperatures

as shown in Figure 6.3. The sharp increase of cavity volume within the first minute of annealing implies that the aggregation of small bubbles in the damaged region occurs very rapidly. Indeed, TEM micrograph images have shown that spherical-like cavities with an average diameter of 8 ~ 9 nm are already present in a sample with an implanted dose of $1\times10^{16}/cm^2$ followed by 30 seconds of RTA at 800 °C [87]. The significant increase in cavity diameter was also observed in a higher implanted dose ($5\times10^{16}/cm^2$) study [80]. Fukarek and Kaschny *et al.* [80] found that only small changes in cavity size were detected in the annealing period between 30 to 300 seconds and that the total volume decreases for longer annealing times. They hypothesized that the high He gas pressure within the small bubbles is the driving force behind the fast He release and the sharp increase in the total cavity volume at the very initial stage.

In light of the above arguments, the total amount of He gas retained in the bubbles, as a function of annealing temperature and time, is the key parameter that determines the cavity size and density after the thermal treatment. However, a model that precisely predicts the retained fraction is not available due to the difficulty in modeling the He-He interaction for various bubble sizes. But referring to some of the attempted works [85], [98], [112], one can anticipate that a small effusion rate is present in the case of 700 °C annealing, while for 1000 °C enormous He out-diffusion within a short period is expected. This results in the different void growth routes for the three annealing temperatures seen in Figure 6.3. The slow effusion rate at low temperatures leads to a better gas confinement and prolongs the growth period, as seen in the 700 °C annealing (the presence of He atoms in bubbles tends to stabilize the open volume defects and enhances the bubble coalescing process). In the case of higher temperature anneal, larger

gas out-diffusion rate gives rise to empty voids easily, thus shrinking voids are observed as a result of recombination with displaced Si atoms. This phenomenon is found in both of the high temperature annealings and it is especially true in the case of 1000 °C, where the total out-diffusion of gas takes place before the formation of large stable cavities (in the period less than 1 minute). Therefore, only small voids were formed.

To summarize, the void evolution process can be classified into three phases. First, clusters of He_nV_m complexes or small bubbles form at the very beginning of the annealing process. In this stage, due to the limited amount of empty space present in the damage region, structure volume transformation occurs as the aggregation of He atoms and He_nV_m defects, creating extra space to accommodate all the existing He atoms. This results in ejection of Si atoms from the cavity to the surrounding medium and formation of dislocation loops adjacent to the cavity. Second, as the annealing process proceeds, the effusion of He gas from bubbles starts until an equilibrium pressure condition is reached. The bubble aggregation in this phase is believed to be mainly due to the migration and coalescence mechanism that is driven by the motion of Si atoms on the inner surface of the cavity and leads to the dissolution of small bubbles and the growth of the central large cavity in each cluster. The increment in cavity volume or *S*-parameter for the case of the 800 °C annealing in the period between 1 to 10 minutes should be attributed to the migration of coalescence of small bubbles. Further He out-diffusion leads to a slow change in the coarsening mechanism from the migration and coalescence of small bubbles to Ostwald ripening. In the third and final stage, the complete out-diffusion of He atoms gives rise to annihilation of the cavities with the displaced Si atoms in the vicinity of the layer.

6.1.2 The effect of annealing ambient: oxygen

It is well established that silicon oxidation causes an injection of self-interstitials and the formation of stacking faults in the substrate bulk [11]. The quantity of *I* and the growth rate of OSF increase with the increase of oxidation temperatures and times. In the absence of a predictive model of the void formation process, and given the lack of experimental data in the literature on void formation and evolution under oxidizing conditions, the effect of the injected I flux on vacancy formation remains unclear. To investigate this effect, part of the void formation study was done in an oxygen ambient. Figure 6.4 shows the normalized *S*-parameters as a function of positron annihilation depth for samples under various oxidation conditions. The void evolutions follow patterns similar to the ones witnessed in the N_2 anneal. A continuous increase and a gradual decrease of cavity sizes is found in the cases of low and high temperature treatments, respectively. For the 800 °C annealing, an increase in cavity volume followed by decrease is also observed. This is clearly illustrated in Figure 6.5.

It has been reported that rapid thermal dry Si oxidation at 815 °C results in an *I* concentration in the region below the oxidizing interface exceeding the equilibrium value by about 20 times [79]. Given this, it is reasonable to assume that the annihilation of small voids and the inhibition of larger ones occur when He^+ implanted Si samples are annealed in an O_2 ambient. However, quantitatively comparing the *S*-parameters in Figure 6.1 and Figure 6.4 for samples annealed at the same temperature and time length, an unexpected outcome is observed. Namely, larger voids were formed in an oxygen ambient as compared to those obtained in a nitrogen ambient, except at 1000 °C. This suggests that interstitial injection enhances the bubble clustering process at low temperatures. The

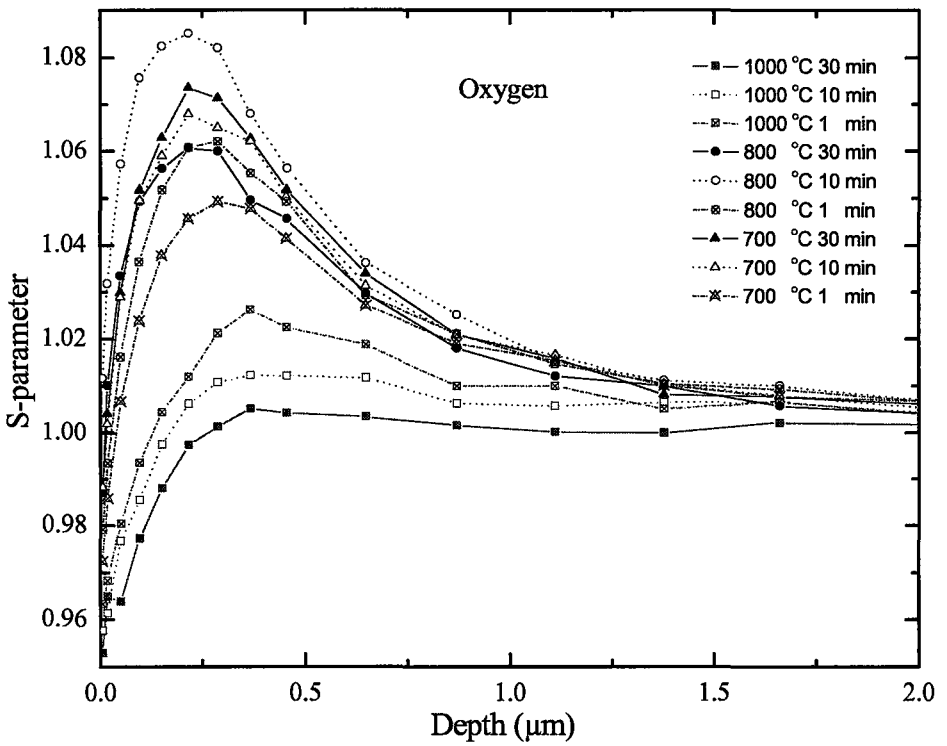

Figure 6.4. Normalized *S*-parameters vs. positron probed depth for samples 1d, 1e, 1f, 2d, 2e, 2f, 3d, 3e, and 3f. All samples were annealed in oxygen RTA ambient for different time lengths and temperatures.

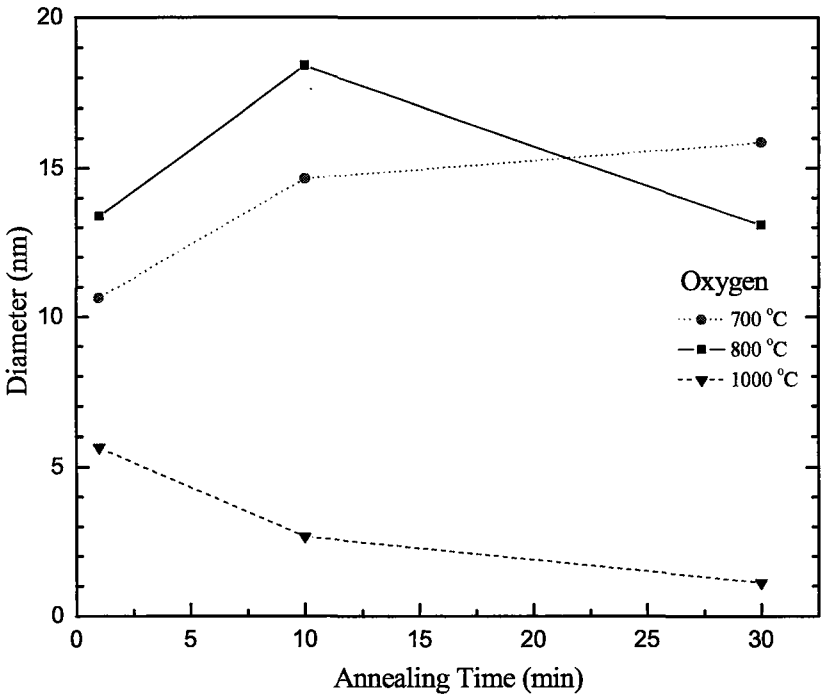

Figure 6.5. Rough estimation of void diameter vs. annealing time for the samples annealed in N_2 ambient.

increase in the *S*-parameters of two typical cases is shown in Figure 6.6. Moreover, carefully examining the growth patterns of the high temperature treatments in Figure 6.5 and Figure 6.3, steeper decreasing slopes were found in the entire process (1 to 30 minutes) for the 1000 °C and beyond 10 minutes for the 800 °C annealed. This suggests that the growth enhancement in the void evolution is only present in the stage where a significant amount of He atoms remains in the bubbles. Alongside the out-diffusion of the gas, a large amount of *I* quickly recombines with the cavities and results in faster void shrinkage.

As mentioned in Chapter 4, in the dose range that we have used in our experiments ($\sim 1\times10^{16}$ cm^{-2}) dislocation loops arise from the bubbles and surround them. It has been argued that these dislocations introduce a "surface ledge" (partial planes of atoms) on the bubble surface. The presence of this ledge enhances the Si surface mobility. Since the mobility of Si atoms on the inner surface of the bubbles is the primary mechanism of bubble migration, the presence of these dislocations enhances the bubble migration [95], thus leading to the formation of larger voids. We hypothesize that the large amount of interstitials diffusing from the oxidizing interface into the bubble layer induces similar ledges on the bubble surface, which enhance the migration and coalescence process in the same manner described above. This is clearly consistent with the rapid increase of cavity volume shown in Figure 6.5 in the period between 1 to 10 minutes for the 800 °C annealing case. Furthermore, helium atoms inside the bubbles would minimize the annihilation between excess interstitials and bubbles in the early annealing stages and stabilize the loops during this stage of the void evolution process.

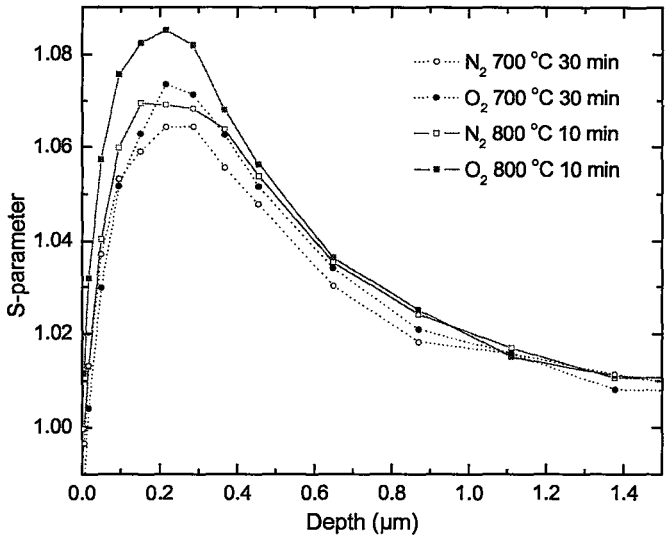

Figure 6.6. Increases in *S*-parameters under O_2 annealing as compared to the results obtained in N_2 ambient.

6.1.3 The effect of ramp rate

Although extensive investigations have been carried out in the past few years, the topic of cavity formation under He^+ implantation into a silicon substrate is a complex phenomenon and little attention has been given to the consequences of varying the ramp rate in rapid thermal treatment. In addition, the results presented above signify that the post-implant anneal temperatures strongly affect the clustering of He_nV_m complexes in the first annealing phase. Thus, clarifying the ramp rate effect allows us to have a deeper level of understanding with regards to the bubble evolution process. Normalized *S*-parameters for the samples annealed at various temperatures and ramp rates are given in Figure 6.7. Note that the significantly smaller S-parameter values shown in the figure, as compared to the ones obtained before, are due to the unstable thermocouple readings (the temperature inside the chamber of the RTA machine is much higher than the set temperature and that the variation is even more difficult to predict at low temperature and short period anneal, as discussed in Section 5.3). A noticeable difference has not been

observed in the cases where small voids were formed. For the case of setting temperature at 800 °C, a small difference is learned. Compared with the un-normalized S-parameters (not shown), the variations could due to the substrate S-parameter that was choose for normalization in each sample. In general, the void formation does not largely affected by the ramp rate, at least in the scope of this study. In fact, a recent investigation has demonstrated that the ramp rate in RTA annealing only affects samples with an implanted dose less than or equal to $5\times10^{15}/cm^2$ [97]. Furthermore, the suggestion that a He atmosphere is formed in the neighborhood of each vacancy cluster in the as-implanted state most likely explains the negligible ramp rate affect on the medium or high implanted dose samples [98]. That is, the He-He interaction in the He_nV_m complexes minimizes the gas out-diffusion from vacancy clusters even if the ramp rate is low. This was illustrated in Figure 4.1, section 4.3. Higher annealing temperatures are needed to reach the out-diffusion peak in high implanted samples.

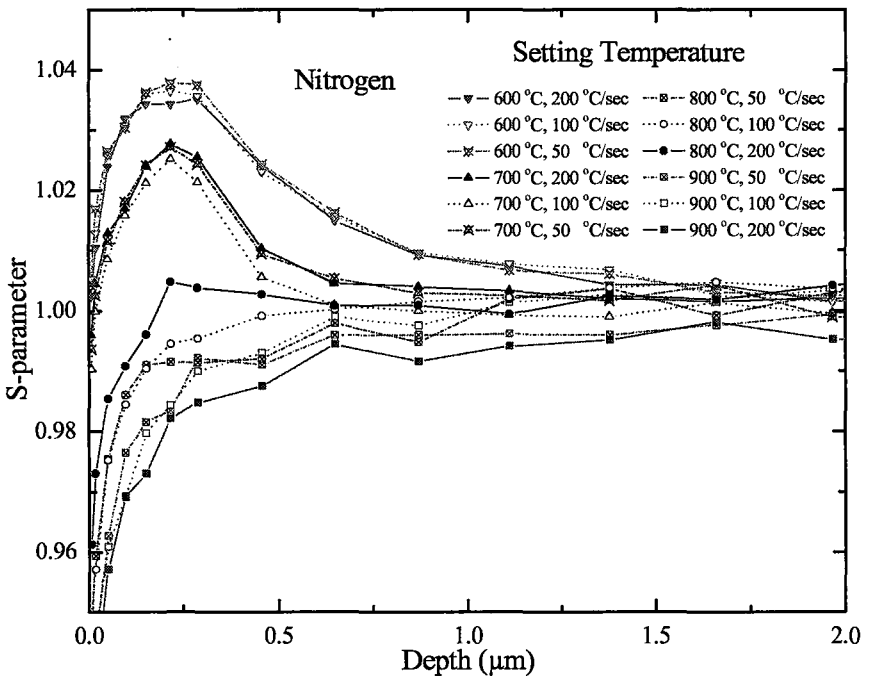

Figure 6.7. Normalized *S*-parameters vs. positron probed depth for samples 4a, 4b, 4c, 5a, 5b, 5c, 6a, 6b, 6c, 7a, 7b, and 7c. All samples were annealed in N_2 RTA ambient for 10 minutes at different ramp up rates.

6.1.4 Summary of void formation experiments

In conclusion, we have studied void formation in Si by implanting He^+ ions at room temperature with energy of 60 keV and a dose of $1\times10^{16}/cm^2$. Analyzing the experimental results, we successfully correlate the cavities volume as a function of annealing temperatures and time. We believe that the transition of void evolution from growing to shrinking depends on the amount of He retained in the cavity and can qualitatively explain the different behavior at different temperatures based on this hypothesis. In addition, the anneals in oxygen ambient show that the supersaturation of I favors the growth of large voids at low temperatures by enhancing the migration and coalescence process. To our knowledge this is the first experimental work investigating the effect of oxidation and interstitial injection on void formation. Finally we have demonstrated that for the He dose used in our study and the temperature range examined here the RTA ramp rate does not significantly affect void formation.

6.2 Point defect injection during wet oxidation of $Si_{0.92}Ge_{0.08}$

The Doppler broadening analyses of the two SiGe samples at different anneal conditions are shown in Figure 6.8. The S-parameters have been normalized to the bulk value of the unimplanted $Si_{0.92}Ge_{0.08}$ wafer. Sample depth is converted from the probed positron energy using equation 6.1, where the $Si_{0.92}Ge_{0.08}$ density is calculated to be 2.60176 g/cm^3. After the first heat treatment, a 10-minute RTA nitrogen anneal at 800 °C, small voids or vacancy clusters were observed as is clearly indicated in the figure with the S-parameter value close to 1.03. The voids' depth is in the range of 350 to 450 nm

from the surface, which agrees with the SRIM simulation value, where the implanted He dose was found to accumulate at a similar depth (Figure 5.6, chapter 5).

As expected, a high temperature long time anneal (30 minutes at 900°C) is sufficient to allow a nearly complete annihilation of the relatively small and unstable voids formed during the first heat treatment. The likely annihilation mechanism is recombination of the voids with the displaced Si atoms induced during implantation. However, a different phenomenon is observed in the case of wet oxidation (sample B). The magnitude of the *S*-parameter is slightly decreased with respect to the first anneal, but it is much higher than the value obtained from sample A. In addition, upon studying the window parameters of the Doppler broadening plots (not shown), it could be seen that the same type of defects are present in the substrate after different heat treatments (1^{st} anneal, inner N_2 anneal and wet oxidation). This indicates that the large amount of vacancies remaining in the sample B after the wet oxidation must have resulted from vacancy injection during the oxidation process, and that it prevented the complete annihilation of the small voids.

To ensure the accuracy of the oxidation process, a small piece of a Cz Si sample with {100} orientation and resistivity of ~ 1 Ω·cm was oxidized together with sample B. The oxide thicknesses and indices of refraction were found to be 37 nm, 1.46 and 98 nm, 1.43 for the Si and SiGe samples, respectively. The oxide thicknesses are confirmed to comply with literature values for both samples. By simulating the SiGe oxidation process, a negligible amount of mixed oxide and a Ge-rich layer with a peak concentration up to 50 % were found [8]. In addition, the simulation result showed that the Ge content in the enriched layer gradually decreases to the bulk value within a thickness of 20 nm.

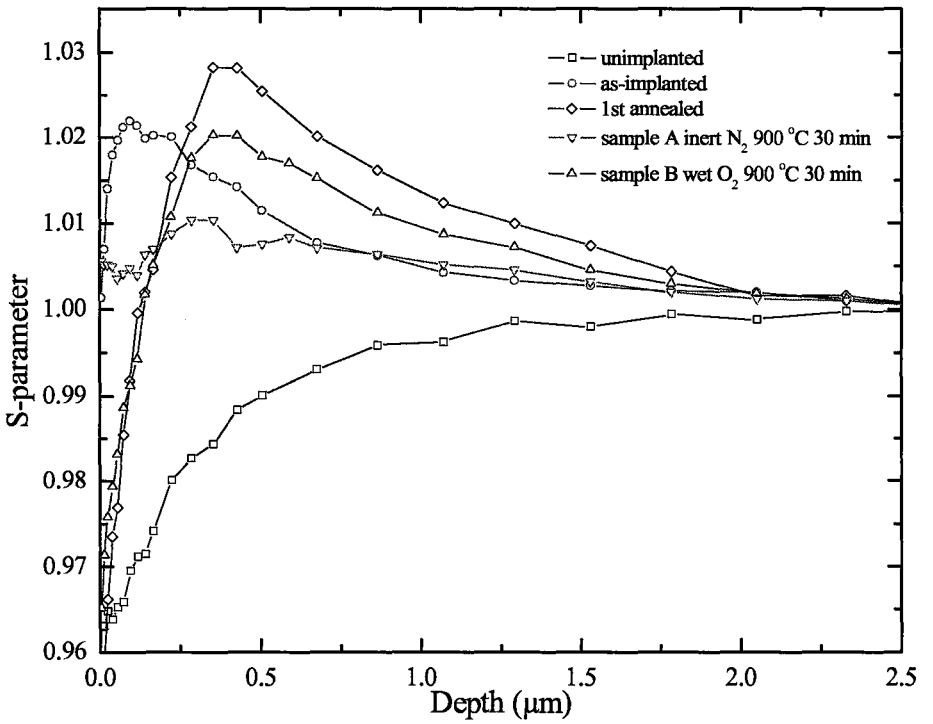

Figure 6.8. Normalized positron *S*-parameter vs. annihilation depth for $Si_{0.92}Ge_{0.08}$ samples at different annealing stages. Sample A and B were annealed in inert and wet ambiences respectively subsequent to the 1st annealed.

It was previously discussed that the self-injection in Si oxidation is caused by the stress accumulated in the oxide transition region and the lack of free space for the newly formed oxide at the SiO_2/Si interface. Any modification of the interfacial properties results in changing the defect generation mechanism and the oxidation kinetics. This has been demonstrated in the dry oxidation of Si with the incorporation of fluorine [51] and chlorine [54], which in both cases were found to have growth rate enhancement and supersaturation of *V*. Based on this argument and our result of *V* injection during SiGe oxidation, the presence of Ge atoms at the oxidizing interface is most likely the cause of stress relief that reduces the requirement for free volume formation.

The decrease in the index of refraction in our study, 1.46 (Si) to 1.43 (SiGe), is also consistent with structure relaxation in the oxide layer of the SiGe samples, which

implies less or stress at the interface than is the case in pure Si. Indeed, the idea of stress relief was proposed by LeGoues et al., but only with the considerations of the difference in binding energy (Si-Ge vs. Si-Si) and in atomic sizes (Si vs. Ge) [6]. In our opinion, the temporary incorporation of Ge into the oxidation process, forming GeO or GeO_2, followed by Si replacing Ge in the oxide is also one of the factors leading to a change in the defect generation mechanism. One can imagine that the breaking of the unstable Ge-O and Si-Ge bonds leads to the destruction of the short range pseudo-crystalline transition structure and the reduction in the oxide viscosity that is required for the free volume creation. Therefore, the transition layer is minimized or completely eliminated in the case of SiGe oxidation. Further, the dangling Si-O- and O-Si- bonds are likely to enhance the insertion of Si or oxygen atoms into the oxide network thus increasing the oxidation rate.

In spite of the above assumptions, the suppression of self-interstitials does not occur simultaneously with the starting of the oxidation process, especially for alloys with low Ge percentage. This has been demonstrated by Napolitani et al. [79] in an investigation of dry SiGe (11% to 15% of Ge) oxidation. The *I* supersaturation was observed at the initial oxidation stage and gradually decreased to the equilibrium value within the first 10 to 20 minutes, depending on the Ge content in the alloy. The authors suggested that the ejection of Si atoms from the oxidizing interface remained throughout the entire process as in the case of Si oxidation. However, they suggest that the formation of a Ge-rich layer caused a change of the *I* injection direction, whereby the ejected Si atoms diffuse into the oxide layer rather than the substrate bulk. This is not sufficient to explain our data where the sizes and concentrations of voids in the oxidized sample

relative to the sample annealed in an inert ambient strongly suggest a flux of vacancies not merely suppression of interstitial injection.

In summary, we have shown that thermal wet oxidation of $Si_{0.92}Ge_{0.08}$ results in the injection of vacancies, contrary to what happens in the wet oxidation of pure Si. This change in point defect generation is likely related to the accumulation of Ge atoms at the oxidizing interface and the formation of a Ge-rich layer. As the percentage of Ge in the enriched layer increases, stress that is often found in Si oxidation is mitigated by the replacement of Ge in the oxide by Si. The weaker Si-Ge bonds lower the oxide formation energy and cause a reduction in the oxide viscous flow that is required for the creation of free volume. In addition, the piling up of Ge atoms at the interface further assists the generation of V, where the formation energy of V is dependent on the near neighbor atoms (section 2.6). The injection of V also gives way for the explanation of the formation of the epitaxial Ge-rich layer, indicating that the regrowth of the Ge-rich layer at the interface is mainly attributed to the recombination of Ge atoms with the vacancy flux.

Chapter 7

Suggestions for Future Work

7.1 Voids formation by helium implantation

We have studied void formation in a silicon substrate by way of an implanted intermediate helium dosage and subsequent high temperature treatments. By varying annealing conditions such as temperature, time length, ramp rate and ambient, systematic observation of the change in cavity size has been reported. The competition between the clustering of He_nV_m complexes and the annihilation of vacancy defects in the very initial annealing stage directly affects the cavity size and density in the damaged layer after the thermal treatments. Under prolonged annealing, the amount of gas retained in the cavity determines the transition point at which continuous growth leads to shrinkage of the cavity. In addition, by comparing the results obtained from the nitrogen and oxygen ambients, we conclude that the migration and coalescence of bubbles should be responsible for the small increase observed in the cavity volume, for the period in which a large fraction of He atoms still remain in the cavity.

Further exploration of the topic is necessary in order to adopt this technique into silicon technology, for example to achieve gettering of transition metals in VLSI design and for reduction of unintentional parasitic transistor gain in power devices. A model that can predict the void size and density in a buried layer as a function of implant dose, energy, and annealing temperature and time will definitely improve the accuracy of fabrication steps and enhance the production yield. However, the absence of a model that accurately captures He desorption at high temperatures makes it difficult to have a

complete picture of the void evolution process. In addition, the presence of voids in the substrate will upset the defect concentration and affect dopant diffusivity, which might lead to the destruction of the geometric structure of a design. Therefore, future work should further explore the void evolution process, and in particular identify the physical processes governing void formation in inert vs. oxidizing ambient.

7.2 SiGe oxidation

In the SiGe point defect study, we have given the first direct demonstration that wet oxidation of SiGe results in the injection of vacancies rather than interstitials. A flux of V is believed to be generated at the oxidizing interface and diffuse to the substrate bulk preventing the complete annihilation of the small pre-existent voids. We suggest that the change in point defect generation is due to the accumulation of Ge atoms at the oxidizing interface, which significantly reduces the interfacial stress and the oxide viscosity flow, lowering requirement for the free volume formation as compared to the case of silicon oxidation. Furthermore, the large amount of V not only assists the upward diffusion of silicon atoms through the Ge-rich layer to the interface sustaining the formation of pure SiO_2, it also is responsible for the formation of the epitaxial Ge rich layer as a result of vacancies recombination with piled-up Ge atoms. Moreover, the relief of interface stress and the generation of V flux give an explanation for the long term growth rate enhancement in wet oxidation.

Despite the successful demonstration of change in point defect generation, the desired incorporation of SiGe into Si-based technology makes it necessary to have a deeper level understanding of the phenomenon. Further investigation such as quantifying

the vacancy flux in wet and dry SiGe oxidation under various experimental conditions is needed, i.e. different temperatures, pressures, and Ge percentages in the alloy. By doing this, a correlation between the oxide growth, the oxidizing interface properties and the amount of V that are generated can be drawn. This will implicitly verify the replacement mechanism, which we suggest it is the main factor that induces the vacancy generation and the oxide growth rate enhancement. Furthermore, by utilizing surface treatment (oxidation), the precise identification of dopant diffusion profile in the material system can be achieved with carefully designed experiments. This helps to simplify the integration of SiGe into Si technology by updating the TCAD models to ensure accurate predictions in modern fabrication process.

Reference:

[1] Paul, D. J., *Semicond. Sci. Technol.*, Vol. 19, pR75-R108, 2004

[2] Bublik, V.T., Gorelik, S. S., Zaitsev, A. A. and Polyakov, A. Y., *Physica Status Solidi B*, Vol. 65, pK79-84, 1974

[3] *Silicon-Germanium Heterojunction Bipolar Transistors, Cressler*, J. D. and Niu, G. F., Artech House, Inc., Norwood, MA, 2003

[4] V. Raineri, J. Appl. Phys., Vol. 78, p3727, 1995

[5] Spadafora *et al.*, Mat. Sci. Semi. Proc., Vol. 8, pp219, 2005

[6] LeGoues et al., J. Appl. Phys., Vol. 65, pp1724, 1989

[7] Kilpatrick *et al.*, J. Appl. Phys., Vol. 81, pp 8018, 1997

[8] Rabie et al., J. Appl. Phys., Vol. 98, p074904, 2005

[9] M. Alatalo, M. J. Puska, and R. M. Nieminen, Phys. Rev. B, Vol. 46, p12806, 1992

[10] V. Raineri, M. Saggio and Rimini E., J. Mater. Res., Vol. 15, p1449, 2000

[11] Fahey *et al.*, Rev. Mod. Phys., Vol. 61, p289, 1989

[12] Gosele, U. and Tan, T.Y., Mater. Res. Soc. Symp. Proc., Vol. 14, p45, 1983

[13] Seeger, A. and Chik, P., Phys. Status Solidi A, Vol. 61, p455, 1968

[14] Hu, S. M., Material Science and Engineering Reports R13, p105, 1994

[15] Ural, A., Griffin, P.B. and Plummer, J.D., Appl. Phys. Lett., Vol. 73, p1706, 1998

[16] Ural, A., Griffin, P.B. and Plummer, J.D., Phys. Rev. Lett., Vol. 83, p3454, 1999

[17] Fahey *et al.*, Appl. Phys. Lett., Vol. 54, p843, 1989

[18] McVay, G. L. and DuCharme, A. R., Phys. Rev. B, Vol. 9, p627, 1974

[19] Strohm *et al.*, Physica B, 308-310, p542, 2001

[20] Zangenberg *et al.*, Phys. Rev. Letts., Vol. 87, p125901-1, 2001

[21] Laitinen *et al.*, Phys. Rev. Letts., Vol. 89, p085902-1, 2002

[22] Venezuela *et al.*, Phys. Rev. B, Vol. 65, p193306, 2002

[23] Delph, T. J., J. Appl. Phys., Vol. 83, p786, 1998

[24] Ourmazd *et al.*, Phys. Rev. Letts., Vol. 59, p213, 1987

[25] Fuoss *et al.*, Phys. Rev. Letts., Vol. 60, p600, 1988

[26] Munkholm et al., Phys. Rev. Letts., Vol. 75, p4254, 1995

[27] Shimura et al., Cryst. Res. Technol., Vol. 33, p 637, 1998

[28] Ikarashi, N. and Watanabe, K., Phys. Rev. B., Vol. 62, p 15989, 2000

[29] Kageshima, H. and Shiraishi, K., Phys. Rev. Letts., Vol. 81, p5936, 1998

[30] Uematsu, M. *et al.*, J. Appl. Phys., Vol. 89, p1948, 2001

[31] Tatsumura et al., Phys. Rev. B, Vol. 69, p085212, 2004

[32] EerNisse, E. P., Appl. Phys. Lett. Vol. 35, p8, 1979

[33] Charitat, G. and Martinez, A., J. Appl. Phys., Vol. 55, p909, 1984

[34] Kobeda, E. and Irene, E. A., J. Vac. Sci. Technol. Vol. B5, p15, 1987

[35] Kobeda, E. and Irene, E. A., J. Vac. Sci. Technol. Vol. B6, p574, 1988

[36] EerNisse, E. P., Appl. Phys. Lett. Vol. 30, p290, 1977

[37] Hu, S. M., J. Appl. Phys., Vol. 64, p323, 1988

[38] Kouvatsos, D. *et al.*, J. Electrochem. Soc., Vol. 138, p1752, 1991

[39] Taft, E. A., J. Electrochem. Soc., Vol. 127, p933-4, 1980

[40] Imai, K. and Yamabe, K., J. Appl. Phys., Vol. 83, p3849, 1998

[41] Gayathri, N. and Banerjee, S., Appl. Phys. Lett., Vol. 84, p5192, 2004

[42] Lewis, E. A. and Irene, E. A., J. Electrochem. Soc., Vol. 134, p2332, 1987

[43] Ngau et al., J. Electrochem. Soc., Vol. 149, pF98, 2002

[44] Deal, B.E. and Grove, A.S., J. Appl. Phys., Vol. 36, p3770, 1965

[45] Lin et al., J. Electrochem. Soc., Vol. 128, p 1121, 1981

[46] Nicollian, E.H. and Risman, A., J. Electronic Mat., Vol. 17, p263, 1988

[47] Tan, T. Y. and Gösele, U., Appl. Phys. Lett. Vol. 39, p86, 1981

[48] Dunham, S. T. and Plummer, J. D., J. Appl. Phys. Vol.59, p2541, 1986

[49] Hu, S. M., J. Appl. Phys., Vol. 45, p1567, 1974

[50] Kim, U. S. and Jaccodine, R.J., Appl. Phys. Lett., Vol. 49, p1201, 1986

[51] Kim, U. S. and Jaccodine, R. J., Proceedings Of the 6th International Symposium On Silicon Materials Science and Technology: Semiconductor Silicon 1990, p376, 1990

[52] Kazor et al., Appl. Phys. Lett., Vol. 65, p1572, 1994

[53] Jaccodine, R. J. and Kim, U. S., Defects and Diffusion in Silicon Processing. Symposium, p71-6, 1997

[54] Deal, B. E., Hurrle, A. and Schulz, M. J., J. Electrochem. Soc., Vol. 125, p2024, 1978

[55] Murarka, S. P., Phys. Rev. B., Vol. 21, p692, 1980

[56] Hokari, Y. and Shiraki, H., Jpn. J. Appl. Phys. Vol. 16, p1899, 1977

[57] Hess, D. W. and Deal, B. E., J. Electrochem. Soc., Vol. 124, p735, 1977

[58] Uematsu *et al.*, Jpn. J. Appl. Phys. Vol. 41, p2455, 2002

[59] Hu, S. M., Appl. Phys. Letts, Vol. 27, p165, 1975

[60] Leroy, B., J. Appl. Phys., Vol. 50, p7996, 1980

[61] Cahill, D. G. and Avouris Ph., Appl. Phys. Lett., Vol. 60, p326, 1992

[62] Hu, S. M., in *Defects in Semiconductors*, edited by Narayan, J. and Tan, T. Y., North-Holland, New York, p333,1987

[63] Law, M. E., Haddara, Y. M. and Jones, K. S., J. Appl. Phys., Vol. 84, p3555, 1998

[64] Holland, O. W., White, C. W., and Fathy, D., Appl. Phys. Lett., Vol. 51, p520, 1987

[65] Hellberg et al. I, J. Appl. Phys., Vol. 82, p5773, 1997

[66] Hellberg et al. II, J. Appl. Phys., Vol. 82, p5779, 1997

[67] Frey, et al., J. Appl. Phys., Vol. 74, p4750, 1993

[68] Terrasi et al., Material Science and Engineering B, Vol. 89, p269, 2002

[69] Zhang et al., Thin Solid Films, Vol. 222, p141, 1992

[70] Spadafora et al., Appl. Phys. Letts., Vol. 83, p3713, 2003

[71] Terrasi et al., J. Appl. Phys., Vol. 91, p6754, 2002

[72] Paine, D. C., Caragianis, C., and Schwartzman, A. F., J. Appl. Phys., Vol. 70, p5076, 1991

[73] Nayak, et al., Appl. Phys. Lett., Vol. 57, p369, 1990

[74] Nayak, et al., J. Appl. Phys., Vol. 76, p982, 1994

[75] *Silicon VLSI Technology Fundamentals, Practice and Modeling*, Plummer, J. D., Deal, M. D. and Griffin, P. B., Prentice Hall, Upper Saddle River, N.J., 2000

[76] Choi, et al., J. Appl. Phys., Vol. 90, p5819, 2001

[77] Kilpatrick, et al., J. Appl. Phys., Vol. 93, p4896, 2003

[78] Ahn, et al., Jpn. J. Appl. Phys., Vol. 37, p1316, 1998

[79] Napolitani, et al., J. Appl. Phys., Vol. 97, p036106, 2005

[80] Fukarek, W. and Kaschny, J. R., J. Appl. Phys., Vol. 86, p4160, 1999

[81] Corni, *et al.*, J. Appl. Phys., Vol.85, p1401, 1999

[82] Brusa *et al.*, Phys. Rev. B, Vol.61, p10154, 2000

[83] Fichtner *et al.*, Appl. Phys. Lett., Vol.70, p732, 1997

[84] Kaschny *et al.*, Nucl. Instr. And Meth. B, Vol. 136-138, p583, 1998

[85] Roqueta *et al.*, Nucl. Instr. And Meth. B, Vol. 147, p298, 1999

[86] Frabboni *et al.*, Phys. Rev. B., Vol. 69, p165209, 2004

[87] Fichtner *et al.*, Nucl. Instr. and Meth. B, Vol. 148, p329, 1999

[88] Evans, J. H., Nucl. Instr. and Meth. B, Vol. 196, p125, 2002

[89] Vishnyakov, V. M., Donnelly, S. E. and Carter, G., J. Appl. Phys., Vol.94, p238, 2003

[90] Donnelly, S. E., Vishnyakov, V. M., Birtcher, R. C. and Carter, G., Nucl. Instr. and Meth. B, Vol. 175-177, p132, 2001

[91] Godey *et al.*, J. Appl. Phys., Vol. 87, p2158, 2000

[92] Oliviero, E., Beaufort, M.F., and Barbot, J. Appl. Phys., Vol. 89, p5332, 2001

[93] Oliviero, E., Beaufort, M.F., and Barbot, J. Appl. Phys., Vol. 90, p1718, 2001

[94] Godey *et al.*, J. Appl. Phys., Vol. 87, p2158, 2000

[95] Beere, W. B., Philos. Mag., Vol. 25, p189, 1978

[96] Silva *et al.*, Nucl. Instr. and Meth. B, Vol. 175-177, p335, 2001

[97] Simpson, T. W. and Mitchell, I. V., Appl. Phys. Lett., Vol. 86, p241907, 2005

[98] Cerofolini *et al.*, Phys. Rev. B, Vol. 61, p10183, 2000

[99] Corni *et al.*, Phys. Rev. B, Vol. 56, p7331, 1997

[100] Silva et al., Nucl. Instr. Meth. B, Vol. 219-220, p713, 2004

[101] Raineri, R. and Saggio, M., Appl. Phys. Lett., Vol.71, p1673, 1997

[102] Laakso, A., Saarinen, K. and Hautojärvi, P., Physic B, Vol. 308-310, p1157, 2001

[103] *Positron Annihilation in Semiconductors, Defect Studies,* R. Krause-Rehberg and H.S. Leipner, Springer-Verlag Berlin Heidelberg, Germany, 1999

[104] Mourino M., Lőbl H. and Paulin R., Phys. Lett. A, Vol. 71, p106, 1979

[105] Schultz, P. J. and Lynn, K. G., Rev. Mod. Phys., Vol. 60, p701, 1988

[106] *Identification of Defects in Semiconductors, Volume 51A,* Michael Stavola, Academic Press, San Diego, CA, USA, 1998

[107] *Positron Spectroscopy of Solids,* A. Dupasquier and A. P. Mills, IOS Press, Amsterdam, Netherlands, 1995

[108] MacDonald et al., Nucl. Instrum. and Meth., Vol.153, p189, 1987

[109] Lynn et al., Phys. Rev. Lett., Vol.38, p241, 1977

[110] Knights, A. P. and Coleman, P. G., Defect and Diffusion Forum, Vol. 183-185, p 41, 2000

[111] J. F. Ziegler, J. P. Biersack and U. Littmark, The Stopping and Range of Ions in Solids, Pergamon Press, New York, 1985

[112] Griffioen, C. C., Evans, J. H., de Jong, P. C. and van Veen, A., Nucl. Instrum. Methods Phys. Res. B, Vol. 27, p417, 1987